



HAL
open science

Designing Patterns for DIC with Poisson Image Editing

Y. Shi, B. Blaysat, H. Chanal, M. Grédiac

► **To cite this version:**

Y. Shi, B. Blaysat, H. Chanal, M. Grédiac. Designing Patterns for DIC with Poisson Image Editing. Experimental Mechanics, 2022, 62 (7), pp.1093-1117. 10.1007/s11340-022-00862-6 . hal-03784274

HAL Id: hal-03784274

<https://hal.science/hal-03784274>

Submitted on 22 Sep 2022

HAL is a multi-disciplinary open access archive for the deposit and dissemination of scientific research documents, whether they are published or not. The documents may come from teaching and research institutions in France or abroad, or from public or private research centers.

L'archive ouverte pluridisciplinaire **HAL**, est destinée au dépôt et à la diffusion de documents scientifiques de niveau recherche, publiés ou non, émanant des établissements d'enseignement et de recherche français ou étrangers, des laboratoires publics ou privés.

Designing Patterns for DIC with Poisson Image Editing

Y. SHI, B. BLAYSAT, H. CHANAL, M. GREDIAC[†]

Institut Pascal, UMR 6602, Université Clermont-Auvergne, CNRS, SIGMA Clermont, Clermont-Ferrand, France

[†] *corresponding author, tel: +33 4 73 28 80 77, fax: +33 4 73 28 80 27, michel.grediac@uca.fr*

Keywords

Digital image correlation, Displacement field, Metrology, Pattern optimization, Poisson image editing, Uncertainty quantification

Abstract

Background: The pattern used in DIC directly influences the quality of the measurement obtained with this technique, so it is of prime importance to optimize the geometry of the features characterizing the pattern to achieve the best metrological performance. **Objective:** The primary objective of this study is to quantify the influence of the collinearity between the actual displacement and the pattern image gradient on the systematic and random errors affecting displacement fields measured by DIC. **Methods:** Poisson Image Editing (PIE), a technique borrowed from the image processing community where it was introduced to perform seamless cloning of images, has been employed here to render various patterns whose gradient is globally collinear to the displacement field. Directly integrating the displacement field considered as the image gradient does not lead to a sufficiently contrasted pattern. A texture is therefore superposed to the displacement field before integration. **Results:** Different patterns obtained or not by PIE are compared, and it is shown with suitable simulations performed with synthetic images that rendering a pattern where the image gradient is globally collinear to the displacement significantly reduces the total error affecting the measurements. The value of this improvement depends on the texture added to the displacement field before applying PIE. **Conclusion:**

This study demonstrates that the collinearity between the speckle image gradient and the displacement field reduces the error affecting the displacement fields measured by DIC. It also proposes a route to account for this displacement in the design of an optimized pattern when a priori knowledge on the direction of the displacement is available. If not, it is shown that a small checkerboard inlayed in a larger one leads to a metrological performance much better than that obtained with a classic random pattern, and close to that achieved with an optimized pattern for which the displacement field is accounted for.

1. Introduction

Digital Image Correlation is a full-field measurement technique which has widely spread in the experimental mechanics community. The main reason is that it enables experimentalists to measure, within certain limits, displacement and strain fields on the surface of specimens subjected to various types of tests.

Assessing the metrological performance of this technique has attracted many researchers for the last 40 years, and various parameters influencing this performance have been studied in the literature. The main ones are the subset size, the order of the shape functions modeling the displacement within the subsets, the way camera sensor noise propagates to the final maps, and the strategy employed to minimize the optical residual over the subsets to retrieve the displacement. It seems that the influence of the speckle pattern used to mark the specimens has only recently been addressed in the literature. However, understanding the influence of the pattern characteristics on the errors impairing displacement maps provided by DIC is a chief issue that must be tackled in order to propose patterns which are optimal for such measurements. Several metrics have been proposed in the literature in order to assess the suitability of a given pattern for DIC, the quality of the measurements being estimated by the random and the systematic errors affecting the displacement maps [1]. The most simple quality metrics for speckle patterns rely on relevant geometrical characteristics of the speckles covering the surface of interest such as the mean speckle size, the evenness of the size distribution, the average number of speckles per subset, the standard deviation of the gray level distribution within each subset

or the mean fluctuation of the gray level in each subset [2, 3, 4, 5, 6]. More global parameters have also been introduced in the literature. For instance, Shannon entropy is a quantity reflecting the degree of feature information in a speckle pattern, and it has been observed in [7] that the higher this quantity, the lower the measurement errors. Other relevant parameters rely on the speckle image gradient. Indeed the norm of this quantity is involved in the denominator of different predictive formulas estimating the propagation of camera sensor noise to final displacement maps given by DIC. In this spirit, it is proposed in [8] to consider the Sum of Square of Subset Intensity Gradients (SSSIG) and in [9] the Mean Intensity Gradient (MIG). These quantities must be as high as possible to minimize sensor noise propagation. Features of the auto-correlation function of the speckle image can also be considered as global indicators. For instance, according to [10], the first peak of this function must be as sharp as possible, while the height of the largest secondary peak of this function must be as low as possible in case of large deformation [11]. Some authors also propose to combine some of the quantities defined above to form new and more reliable quality metrics. This is all the more relevant as some criteria, for instance those based on image gradient such as the SSSIG and the MIG, favor high contrasted patterns to minimize sensor noise propagation, but the systematic errors caused by interpolation increase in this case [12]. It is therefore necessary to combine various criteria to find a reasonable tradeoff between contradictory constraints. In [11], it is proposed to consider *i*- the SSSIG, *ii*- the radius of the flat zone surrounding this peak, which corresponds to patterns relatively insensitive to initial guess for the iterative minimization of the optical residual (this zone, called “watershed”, is reported to give optimal patterns correlated to the height of the first peak), and *iii*- the height of the largest secondary peak of the autocorrelation function. This procedure has been extended in [13] to optimize multiscale patterns. In [14], the inhomogeneity of the gray level distribution, the mean square deviation of this distribution and the standard deviation of the speckle particles size distribution have been considered to form a global quality metric. The reader is referred to [15] for a detailed overview on these criteria.

The next step is to resolve what could be considered as an inverse problem, namely how to design a pattern corresponding to a desired value for one of the criteria defined above or for a combination of

some of them. Considering the best possible values for these criteria, answering correctly this question is a critical issue since the response would provide optimal patterns for DIC with respect to the chosen criterion. In [10], speckle patterns are designed in such a way that a sharp auto-correlation peak and a broad correlation margin are obtained at the same time. These patterns exhibit neither feature too small to be resolved by the imaging system nor large featureless zones. In [16], a Gaussian-type power spectrum with adjustable spread, scaling and noise is associated with a phase angle of diameter-controlled speckle pattern in order to drive pattern generation by inverse Fourier transform. Patterns suitable for multi-scale DIC measurements are also generated in [17] directly from an auto-correlation function featuring desired properties. In [18], it is proposed to consider checkerboards as ideal patterns because they lead to the highest possible SSSIG and MIG, and thus to the lowest impact of sensor noise in displacement maps. This type of pattern being periodic, the minimization of the optical residual is switched from the spatial domain to the frequency domain, which causes the interpolation errors as well as the bias due to the pattern itself to virtually vanish [19, 20, 21], and leads the minimization procedure to be quasi-direct [22, 23], thus dramatically speeding up the numerical resolution of the problem.

In this context, the objective of this paper is to investigate a route, which seems not to have been explored so far since it consists in adapting to the sought displacement field the pattern deposited onto the surface of the specimen. Indeed, DIC relies on a minimization procedure of the so-called optical residual which is, under its simplest form, the squared difference between the gray level distribution within a subset considered in the reference image on the one hand, and its counterpart in the image of the deformed pattern on the other hand. This minimization procedure is performed iteratively with respect to the sought displacement. It can be shown that the quality of the gradient descent is driven by the collinearity between image gradient and actual displacement. In other words, the better this collinearity, the higher the robustness of the minimization procedure, thus the better the quality of the result found at the end. The first motivation of this work is therefore to define patterns, which are tailored to a given DIC problem so that image gradient and displacement are as collinear as possible,

to observe if the quality of the measured displacement fields is really improved, and to quantify this improvement in this case. Some a priori knowledge on the sought displacement is therefore required. This point could be considered as contradictory with the fact that the displacement field is the sought quantity. However, this remark also holds for the integrated version of DIC, for which the displacement field is described by a type of function known a priori. DIC provides in this case the parameters which govern the solution, which automatically improves the robustness of the latter. Refs [24] and [25] are typical examples. In the first reference, the closed-form solution for the displacement field obtained within the framework of elasticity in the vicinity of a crack tip is used [26]. In the second reference, the displacement field is assumed to be Euler-Bernoulli-like to measure the warping of a workpiece caused by the release of residual stresses during milling. Another route to get a priori knowledge on the displacement field is to perform a dummy test with a classic version of DIC applied with a classic random speckle pattern deposited onto the specimen, or to perform instead a finite element calculation. This dummy test or FE calculation would then provide a first approximation of the displacement field. This first estimate could then be leveraged to define a pattern, which would be used to mark another specimen and perform a second test. With this second test, the errors caused by the pattern in the DIC calculations would be minimized.

The paper is organized as follows. The statement of the problem is first briefly given in Section 2, with an emphasis on the impact of collinearity between image gradient and actual displacement on the quality of the final result. The way the pattern can be suited to a given displacement field is discussed in Section 3. The technique adopted here is the so-called Poisson Image Editing. The different patterns discussed in this study are then presented in Section 4. They are split into two types. The first one gathers patterns which do not depend on the displacement field, which is not the case of the second type. A synthetic problem, namely an open-hole specimen subjected to a tensile test, is therefore chosen to illustrate the approach. The metrological performance of DIC applied on these different patterns is then discussed in Section 5, and the improvement brought about by patterns accounting for the displacement field in their definition is estimated. The results of some experiments

are finally presented in Section 6.

2. Why to use a pattern such that image gradient is collinear to the displacement ?

In [20], the authors propose a formula, which directly gives the link between displacement uncertainty and image gradient. Under mild assumptions, the following equation is established in this reference:

$$\sigma = \frac{1}{\cos\theta(\mathbf{u}_{DIC}, \nabla\mathcal{I})} \sqrt{2\eta^2 \|\Sigma\|_{max}} \quad (1)$$

where:

- σ is an upper bound of the standard deviation of the noise affecting the displacement maps;
- η is the standard deviation of the "image noise", this image noise being here assumed to have the same standard deviation at any pixel;
- $\|\cdot\|_{max}$ is the max norm of a matrix, thus for any matrix A of dimensions $M \times N$, $\|A\|_{max} = \max_{i,j} |A_{ij}|$;
- Σ is a 2×2 matrix such that $\Sigma = (\int_{\Omega} \nabla\mathcal{I} \otimes \nabla\mathcal{I} dS)^{-1}$, where \mathcal{I} is the reference image, Ω the subset and \otimes the outer product.

Equation 1 above can be regarded as a weighted form of the image noise propagation model proposed in [27], the weights being equal to the inverse of the cosine between image gradient and displacement provided by DIC. The better the collinearity, the higher the value of this cosine and the lower the noise propagation, thus image gradient and displacement should be as collinear as possible. It is also worth noting that the angle between image gradient and actual displacement is involved in the model predicting the so-called pattern-induced bias (see details in [21]) but this link is not explicit, so it can only be said that collinearity between image gradient and actual displacement influences this type of systematic error.

3. Poisson Image Editing: a tool to define patterns suited to a given displacement field

3.1. Principle

The problem at hand is to define a pattern in such a way that the orientation of the image gradient is as collinear as possible to the displacement, the direction of the latter at any point being a priori known. However, other constraints shall also be accounted for to obtain high-quality DIC measurements. In particular and as recalled in the introduction, sensor noise propagation is inversely proportional to image gradient, so the latter quantity must be sufficiently high to limit noise propagation. We will see in Section 4 below that directly integrating the displacement field considered as the image gradient leads to a rather smooth image. As such, it cannot be used as a pattern deposited onto a specimen for DIC measurement. A texture shall therefore be superimposed to this displacement. The main problem is to seamlessly account for the high-contrast texture while integrating the displacement, the latter giving the global direction of the image gradient. The method employed here to reach this goal is inspired by that proposed in [28], where images are touched up by manipulating the gradient field of the luminance image, more precisely by attenuating the magnitude of large gradients, and then resolving the Poisson equation to render the modified image. This approach was then extended in [29], where the so-called Poisson Image Editing (PIE) was introduced to perform seamless cloning of images. This method is now very popular in the image processing and computer graphics communities, as illustrated by various types of examples dealing for instance with local illumination changes [30], concealment [31], object insertion [32], image stitching [33], texture flattening [29] or seamless tiling [29]. These examples illustrate the versatility and the power of PIE to clone images. However, it seems this technique has never been used so far to define patterns for DIC. We therefore briefly explain below how it works. The procedure consists in searching for a function \mathcal{I} whose gradient is the closest, in the least squares sense, to a given “guidance vector field”, a term coined by the authors of the seminal paper for this approach [29]. This guidance vector field, denoted here by \underline{g} , is supposed to be differentiable. This leads to the following variational problem

$$\min_{I \in \mathcal{C}^2(\mathcal{R})} \int_{\mathcal{R}} \|\nabla I - \underline{g}\|^2 dx \quad (2)$$

where :

- \mathcal{R} represents the image domain;
- $\mathcal{C}^2(\mathcal{R})$ represents the set of real functions twice differentiable over \mathcal{R} ;
- \mathcal{I} is the unknown image to be retrieved.

Neumann boundary conditions are considered in [28], while Dirichlet ones are used in [29]. Since we have here an a priori knowledge on the displacement and since the latter serves as a guide for constructing the desired image \mathcal{I} , it seems logical to use here Neumann boundary conditions.

The unique solution \mathcal{I} of this minimization problem satisfies the Euler-Lagrange equation associated to this variational problem. This leads to the so-called Poisson equation [28]:

$$\Delta \mathcal{I} = \text{div } \underline{g}, \quad (3)$$

with homogeneous Neumann boundary conditions, which write as follows:

$$\nabla \mathcal{I} \cdot \underline{n} |_{\partial \mathcal{R}} = 0, \quad (4)$$

where $\partial \mathcal{R}$ is the boundary of the domain \mathcal{R} over which the image is defined. Equation 3 is nothing but the so-called Poisson equation, which is of broad utility in various branches of physics.

3.2. Resolution

Various numerical strategies have been proposed in the literature to resolve the problem defined above. Since we deal here with complete images which are rectangular by essence, the Fourier approach described in [34, 32] is well adapted. The main steps of this method are given in this section.

Since the procedure relies on the Discrete Fourier Transform (DFT), it is recalled that the DFT of any periodic bidimensional function X , which represents here an image defined over a grid of dimensions $M \times N$, is defined as follows :

$$\widehat{X}(u, v) = \sum_{x=0}^{M-1} \sum_{y=0}^{N-1} X(x, y) e^{-2\pi i \left(\frac{xu}{M} + \frac{yv}{N} \right)}, \quad (5)$$

with $i^2 = -1$, and the Inverse Fourier Transform :

$$X(x, y) = \frac{1}{M \times N} \sum_{u=0}^{M-1} \sum_{v=0}^{N-1} \widehat{X}(u, v) e^{2\pi i \left(\frac{xu}{M} + \frac{yv}{N} \right)}. \quad (6)$$

It is also recalled that the Fourier transforms of the partial derivatives of any function X are merely equal to :

$$\frac{\partial \widehat{X}}{\partial x}(u, v) = \frac{2\pi i u}{M} \widehat{X}(u, v) \quad \text{and} \quad \frac{\partial \widehat{X}}{\partial y}(u, v) = \frac{2\pi i v}{N} \widehat{X}(u, v). \quad (7)$$

The guidance vector \underline{g} being in general not periodic, the first step is to define from \underline{g} a so-called “extended guidance vector” denoted by $\underline{\mathbf{G}}$, which is periodic. This is made by duplicating both the components of \underline{g} by applying a mirror symmetry to each of them, with respect to a vertical line for g_x and an horizontal line for g_y , see Figures 1-a and -b. This leads the extended guidance vector $\underline{\mathbf{G}}$ to be periodic, see Figure 1-c. Following the procedure defined in [35], a zero padding is also applied so that the Neumann boundary conditions are satisfied.

\mathcal{J} is obtained by taking the DFT of both sides of the Poisson equation given in Equation 3 applied to \mathcal{J} instead of \mathcal{I} . This leads to :

$$\left[\left(\frac{2\pi i}{M} u \right)^2 + \left(\frac{2\pi i}{N} v \right)^2 \right] \widehat{\mathcal{J}}(u, v) = \left(\frac{2\pi i}{M} u \right) \widehat{G}_x(u, v) + \left(\frac{2\pi i}{N} v \right) \widehat{G}_y(u, v). \quad (8)$$

The DFT coefficients characterizing the Fourier transform of the solution of the Poisson equation are therefore defined by :

$$\widehat{\mathcal{J}}(u, v) = \begin{cases} \frac{\left(\frac{2\pi i}{M} u \right) \widehat{G}_x(u, v) + \left(\frac{2\pi i}{N} v \right) \widehat{G}_y(u, v)}{\left(\frac{2\pi i}{M} u \right)^2 + \left(\frac{2\pi i}{N} v \right)^2}, & u = 1 \cdots (M-1), v = 1 \cdots (N-1), \\ \mathcal{J}(0, 0) \in \mathbb{R}, & u = 0, v = 0. \end{cases} \quad (9)$$

$\mathcal{J}(0, 0)$ is a constant of integration. It is chosen to be equal to the mean value of the output image

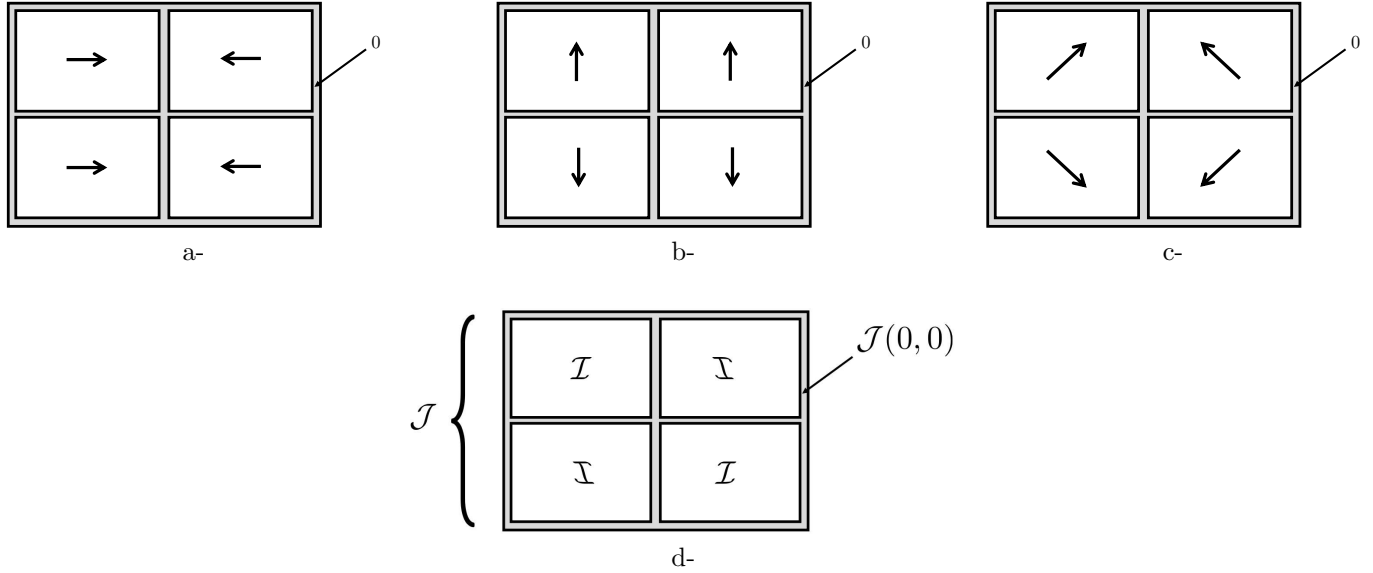


Figure 1: Schematic view illustrating the construction of \mathbf{G} , \mathcal{J} and \mathcal{I} . a- Mirror symmetry + zero padding applied to g_x to construct \mathbf{G}_x . b- Mirror symmetry + zero padding applied to g_y to construct \mathbf{G}_y . c- resulting vector \mathbf{G} . d- Image \mathcal{I} is obtained by considering the top right quarter of \mathcal{J} and removing the zero padding.

\mathcal{I} . Taking the inverse Fourier transform of $\hat{\mathcal{J}}$ provides an image denoted by \mathcal{J} , and this “big” image contains the sought image \mathcal{I} as well as its duplicates. \mathcal{I} is therefore extracted from \mathcal{J} by removing the duplicates and the zero padding.

4. Patterns considered in this study and quality assessment of the displacement field returned by DIC

4.1. Procedure

Different patterns were studied here. Two cases will be distinguished. Patterns of “Type 1” which are “classically” defined, thus independently of the actual displacement field, were considered first. The actual displacement field was then taken into account in the design process of the patterns of “Type 2”, so that the gradient the pattern image is as collinear as possible to the direction defined by the actual displacement. The procedure described in Section 3 above was used to design these latter patterns.

These different patterns were considered in turn to define reference images. These reference images were then deformed through a given displacement field described in Section 4.5. The gray value at the pixels of the deformed images were obtained by numerically integrating the value of the gray level in

Technique used	2D image correlation
Subset Size	21×21 pixels
Shift	1 pixel
Shape function	First-order
Interpolation function	Spline polynomial
Correlation criterion	SSD*
Pre-smoothing applied to the images	None
Camera	8 bit, 6576×4384 pixels

Table 1: Experimental DIC settings and performances. * SSD: Sum of Squared Differences.

the reference image, at the points which are the preimages of the 3×3 Gauss points regularly spaced in any pixel of the image of the deformed configuration, and by taking the closest integer value of the result. The coordinates of the preimages were obtained by using a fixed-point algorithm. Note that when the gray level distribution in the reference images was given by a closed-form equation, such as for Patterns #2-4 described below, the gray level at any pixel of the reference images was also obtained by numerically integrating the value returned by the closed-form expression at the Gauss points, so that the procedure used to obtain these images was the same as that used for the other images.

DIC was applied by using first-order subset shape functions. The subset size was equal to 21 pixels and the shift between two measurements was set to one, as in recent studies dealing with the ultimate performance of DIC, see [36] for instance. The parameters which govern the DIC calculations are gathered in Table 1, as suggested in [37].

4.2. Estimation of the systematic and random errors for each pattern.

Any pair of reference/deformed image was processed by DIC and two types of errors, namely the systematic error and the random error, were evaluated. The systematic error was assessed by comparing the displacement field returned by DIC and a reference displacement field. However, DIC cannot do better than providing the actual displacement field *convolved* by a Sawitzky-Golay filter, as stated in [38], numerically verified in [39] and finally demonstrated in [21]. This Savitzky-Golay filter is driven by the order of the subset shape function and by the size of the subset used in the DIC calculation [40]. Consequently, the systematic error was estimated by subtracting pixelwise the displacement field given by DIC and the reference displacement field convolved by the Sawitzky-Golay

filter corresponding to the subset size and the degree of the subset shape functions used for the DIC calculations (see Table 1). The mean value of the norm of the vector representing this difference at any pixel enables us to assess the systematic error. This mean value is denoted by M_s . It will be provided in the results presented below.

For each pattern, the random error was estimated by calculating the standard deviation of the difference between the displacement maps obtained with noisy images and their counterparts obtained with noiseless images. This standard deviation was estimated pixelwise for both U_x and U_y by using 100 pairs of reference/deformed images, each of them being affected by different copies of the noise. The global standard deviation for all the images, denoted by σ_g , was finally estimated by considering the standard deviation of the norm of the random part of the displacement at any pixel, thus:

$$\sigma_g = \sqrt{\frac{\sum_{i=1}^M \sum_{j=1}^N \sigma_x^2(x_i, y_j) + \sum_{i=1}^M \sum_{j=1}^N \sigma_y^2(x_i, y_j)}{M \times N}} \quad (10)$$

where $M \times N$ is the size of the images, σ_x and σ_y represent the standard deviation of the displacements U_x and U_y along the x - and y -directions, respectively. x_i and y_j , $i = 1 \dots M, j = 1 \dots N$ are the coordinates of the pixels where these two quantities are estimated. The noisy images were obtained by adding a heteroscedastic noise to reliably mimic typical sensor noise of actual linear cameras [41, 42]. In this case, the variance σ^2 of the camera sensor noise is an affine function of the brightness s , thus $\sigma^2 = a \times s + b$. We have here $a=0.0342$ and $b=0.2679$ to be consistent with the values already used in the DIC Challenge 2.0, [43] for instance. Finally, the Root Mean Square Error (RMSE) defined by $RMSE = \sqrt{M_s^2 + \sigma_g^2}$ was calculated and considered as a global indicator of the performance of each pattern.

The two types of pattern considered in this study are now described in turn in the following sections.

4.3. Case 1: patterns of Type 1 designed independently of the actual displacement field

4.3.1. Pattern #1: “classic” speckle

Random speckle patterns are generally used for DIC measurements. According to [2], a good speckle pattern should be highly contrasted, stochastic and isotropic. We consider here the speckle

represented in Figure 2-a as a typical example.

Recent open-source tools have been recently proposed in the literature to design and print random speckle patterns suitable for DIC, see [44, 45, 46] for instance. We employed here the speckle image rendering program described in [46] to obtain a speckle image. This image was then integrated by using the numerical procedure described in [47], apart from the fact that 3x3 Gaussian numerical integration was performed instead of a Riemann sum because the former is expected to be more accurate than the latter. The reference speckle image was not deformed with the procedure described in [47] because this latter technique is only available for random speckle patterns and not for periodic ones such as those discussed in this study (checkerboards for instance). The same procedure was therefore used to obtain the whole set of eight image patterns for the sake of consistency. It can be checked that as suggested in [48, 49], the dots are sampled with about 3 pixels, and choosing a subset size of 21 pixels leads to have about 3 dots in average along each direction.

4.3.2. Pattern #2: speckle optimized according to [10]

The distribution of the dots in the preceding pattern is random. It is somewhat arbitrary to choose this one instead of any other that the reader could consider as being better. Hence we chose here a random pattern generated with the procedure proposed in [10] since such patterns are often considered as optimal in the DIC community. Such a gray level distribution, denoted here by I_{spk_1} , is represented in Figure 2-b. It was obtained by using the rendering program used in [50]. The `specklesize` parameter driving the fineness of the texture was chosen to be equal to 6 pixels. It can be seen on the closeup view that this type of pattern is random despite its marbled aspect.

4.3.3. Pattern #3: Checkerboard

A good pattern should be highly contrasted. This can be achieved with neighboring pixels featuring the largest possible difference between their gray levels. As discussed in [11], the best pattern with respect to this criterion is the checkerboard. However, the problem is that checkerboards are periodic, so DIC cannot successfully process them if the actual displacement is greater than the period of this pattern. In addition, strong image gradient may potentially increase interpolation bias [12]. We

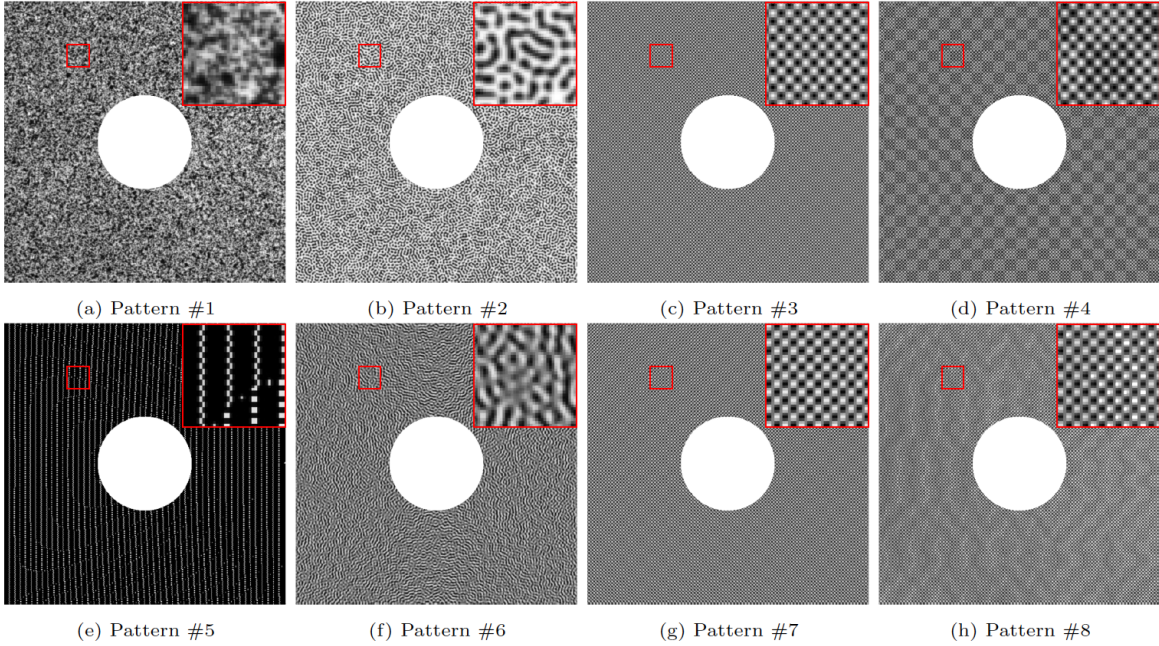


Figure 2: Patterns of types 1 and 2

propose however to examine this case for two reasons. First DIC can be successfully applied on this type of pattern for displacements remaining lower than the period of the checkerboard in amplitude, so this case gives an idea of the ultimate performance that can be achieved with DIC. Second, as discussed in [22] and under mild assumptions, the minimization of the optical residual can advantageously be switched from the spatial to the frequency domain in this case. In this case, the displacement field is not extracted from the images with DIC, but with a spectral method [39, 18, 51]. According to those references, the benefit is threefold. First, displacement greater in amplitude than the period of the checkerboard can be measured. Second, the calculation time is much lower than that of DIC. Third, the metrological performance is similar to that of DIC when the displacement is lower than the period [23], which means that considering this type of pattern gives an idea of the metrological performance which could be reached with a spectral method for any value of the displacement. Investigated further this comparison between DIC and spectral methods is out of the scope of this paper. The reader interested in this comparison is referred to [39, 23, 51].

Checkerboard patterns can easily be generated by using the following periodic function f_{CKB_0}

$$f_{CKB_0}(x, y) = \cos\left(\frac{2\pi}{p_0}x\right) \cos\left(\frac{2\pi}{p_0}y\right) \quad (11)$$

where p_0 is the period of the checkerboard. As discussed in [23, 51], choosing $p_0 = 6$ pixels is a value leading to a good tradeoff between the unavoidable effect of the Point Spread Function of the lens, which decreases the contrast in such images if the size of the dots is small [52], and the need for using low values of the period such as $p_0 = 6$ to get a small spatial resolution. The value of f_{CKB_0} lying between -1 and +1, the gray level distribution for a checkerboard, denoted here by I_{CKB} , is obtained by considering $I_{CKB} = \frac{255}{2} \times (f_{CKB_0} + 1)$ for images defined with a gray depth of 8 bits. The gray value at any pixel of the deformed images was obtained by numerically integrating the value of the gray level given by the continuous function at the 3×3 Gauss points regularly spaced in any pixel of the image, and by taking the closest integer value. A checkerboard obtained with a value of $p_0 = 6$ pixels is shown in Figure 2-c.

4.3.4. Pattern #4: Small checkerboard inlayed in a larger one

As recalled above, pure checkerboard patterns cannot be used with DIC if the sought displacement is greater than its period p_0 . As explained in [11], it is necessary to depart from this pattern so that DIC becomes able to retrieve displacement greater in amplitude than p_0 . We propose here to consider a second checkerboard featuring a much larger period than the one shown in the preceding case, so that coarse graining as described in [53] applied on this pattern provides a first rough but reasonable estimation of the displacement. This rough estimation is then used to fix the initial values for DIC applied without coarse graining. This pattern is merely obtained by keeping the same period of the checkerboard described above (thus 6 pixels), and by slightly enlarging the signal over one half of this period over squares, which are much greater in size than those of this first checkerboard. These bigger squares form another checkerboard with a period p_1 , which is much larger than p_0 . In addition to returning displacements lower in amplitude than $p_0 = 6$ pixels, DIC can reliably return displacement which can at most be equal to the period of the large checkerboard. The period p_1 of this large checkerboard is chosen here to be equal to 8 times that of the small checkerboard, thus to

$p_1 = 6 \times 8 = 48$ pixels. This choice is arbitrary. It is only driven by the maximum displacement that is expected to be correctly measured by DIC.

Denoting by f_{CKB_1} the modulating function of the large checkerboard of period p_1 , f_{CKB_1} has the same expression as f_{CKB_0} in Equation 11 above, but p_0 is changed into p_1 . The following modulating function f_{CIC} has been used to generate the large checkerboard inlaid in the small checkerboard. It depends on both the generating functions of the small and large checkerboards f_{CKB_0} and f_{CKB_1} . Thus

$$f_{CIC} = \begin{cases} f_{CKB_0} & \text{if } f_{CKB_1} \leq 0 \\ \frac{2a}{1+a}f_{CKB_0} + \frac{1-a}{1+a} & \text{if } f_{CKB_1} > 0 \text{ and } f_{CKB_0} > 0 \\ \frac{2}{1+a}f_{CKB_0} + \frac{1-a}{1+a} & \text{if } f_{CKB_1} > 0 \text{ and } f_{CKB_0} \leq 0 \end{cases} \quad (12)$$

a is parameter used to adjust the difference in intensity between the two types of big squares in the large checkerboard of period p_1 . Compared to the precedent case, we can see that this bi-periodic modulation is defined piecewise, with a different affine function over each part of the domain. It can be checked that f_{CIC} lies between -1 and 1, as the other modulation functions defined above. This enables us to define the image I_{CIC} of the large checkerboard inlaid in the small checkerboard by scaling f_{CIC} between 0 and 255, thus $I_{CIC} = \frac{255}{2} \times (f_{CIC} + 1)$. This pattern becomes a mere checkerboard (like Pattern #3) if $a = 1$. We chose here $a = 2$ so that the two types of big squares forming the large checkerboard of period p_1 can easily be distinguished. Figure 2-d shows the pattern obtained with this procedure with $a = 2$.

4.4. Case 2: patterns of Type 2 designed by accounting for the actual displacement field

The idea is now to design patterns suited to a given displacement field by using the procedure explained in Section 3 above. Image gradient shall therefore be taken into account in some way in the design procedure of the patterns. Since these patterns now depend on the displacement field, it is necessary to examine the performance of this approach with an example for which the displacement

is known a priori. We considered here the case of an open-hole specimen subjected to a tensile test. We first briefly recall the closed-form expression for the displacement field obtained in this case. This analytical displacement field will then be used to design the patterns of Type 2 studied here.

4.5. Displacement field under study

4.5.1. Closed-form solution

We consider an open-hole specimen, see schematic view in Figure 3.

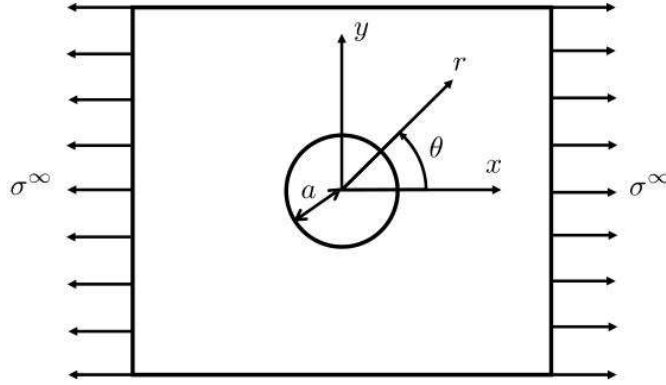


Figure 3: Schematic view of the open-hole specimen under study

We assume that the closed-form expression for \underline{u} is given by the solution obtained by integrating the equations available in elasticity (equilibrium, constitutive equations, relationship between displacement and strain components) in the case of an infinite plate with a hole, this plate being subjected to a homogeneous tensile loading [54]. The specimen shown in Figure 3 is not really infinite in dimension, so the displacement field proposed here is not exactly the one that occurs in the specimen shown in Figure 3. However, this approximation has no impact on the discussion on the results offered below. The closed-form expression for the displacement displacement in polar coordinates $(\underline{e}_r, \underline{e}_\theta)$ is given by [54]:

$$\begin{aligned} u_r(r, \theta) &= \frac{\sigma^\infty}{2E} \left[(1 + \nu) \left(\frac{a^2}{r} + \left(r - \frac{a^4}{r^3} \right) \cos 2\theta \right) + (1 - \nu) r + \left(\frac{4a^2}{r} \cos 2\theta \right) \right] \\ u_\theta(r, \theta) &= -\frac{\sigma^\infty}{2E} \left[(1 + \nu) \left(1 + \frac{a^4}{r^4} \right) r + (1 - \nu) \frac{2a^2}{r} \right] \sin 2\theta \end{aligned} \quad (13)$$

where a is the radius of the circular hole, (r, θ) are the polar coordinates, E is the Young's modulus of the constitutive material, ν its Poisson's ratio and σ^∞ the traction applied along the boundary.

Further calculations being carried out in Cartesian coordinates, the solution given by Equation 13 above shall be converted from polar to Cartesian coordinates, which gives:

$$\begin{cases} u_x = u_r \cos \theta - u_\theta \sin \theta \\ u_y = u_r \sin \theta + u_\theta \cos \theta \end{cases} \quad (14)$$

Note that this solution is given with an origin for the displacement placed at the center of the hole. In practice however, the actual origin depends on the point which remains fixed. Constant values denoted by δ_x and δ_y can therefore be added to u_x and u_y , respectively. This choice is arbitrary but it drives the location of the origin considered for the displacement. These values will be carefully discussed later on in the paper.

4.5.2. Direct integration of the normalized displacement field

Obtaining an image with a gradient which is proportional to the actual displacement field is merely obtained by integrating the two components of this displacement field given in Equation 15. This displacement is normalized to have the same magnitude at any point. Indeed, it is worth remembering that only the direction of the gradient (and not its modulus) is necessary here to align as much as possible the gradient of the pattern with the displacement. The gradient of the sought image denoted by \mathcal{I} is therefore expected to be close if not equal to the guidance vector \underline{g} such that:

$$\begin{aligned} \underline{g} &= \frac{\underline{u}}{\|\underline{u}\|} \\ &= \frac{\underline{u}}{\sqrt{(u_x)^2 + (u_y)^2}} \end{aligned} \quad (15)$$

where $\|\underline{u}\|$ denotes the norm of vector \underline{u} . This integration is performed by resolving numerically the Poisson equation as described in Section 3, and by considering here that the origin is at the center of the hole (thus $\delta_x = \delta_y = 0$). The image \mathcal{I} given by this procedure is depicted in Figure 4.

The main remark is that the contrast of this image is too poor to be used alone as a pattern for DIC measurement. In fact, \mathcal{I} is much too smooth and a texture shall therefore be superimposed in some way. The solution was to increase the local gradient of this pattern while globally keeping the direction given by the gradient of \mathcal{I} . Directly multiplying image \mathcal{I} obtained above by the modulation functions generating checkerboard patterns like Patterns #3 and # 4, namely f_{CKB_0} and f_{CIC} defined in

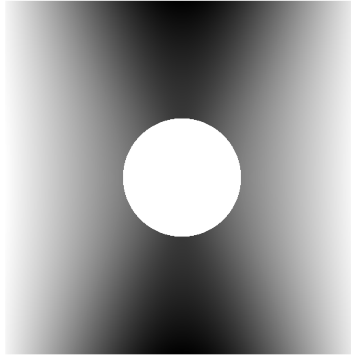


Figure 4: Image \mathcal{I} obtained by considering that the guidance vector is equal to the normalized displacement $\frac{\underline{u}}{\|\underline{u}\|^2}$, \underline{u} being defined by Equations 13-14

Equations 11 and 12, and rescaling the result to have a gray level lying between 0 and 255, automatically increases the local gradient of \mathcal{I} . The problem is however that the amplitude of the contrast in the resulting images would be low in the regions where the amplitude of \mathcal{I} is low itself. The idea was therefore to modulate directly the gradient of \mathcal{I} . Two routes were investigated to reach this goal. The first one was to plot the level lines of \mathcal{I} because the direction of these lines and their normal directly give the local orientation of the displacement. The second one consisted in multiplying in turn the displacement field by the modulation functions of Patterns #3 and 4, and then in integrating the resulting product by using PIE, so that both the effect of the actual displacement and the texture are accounted for in the gradient of the resulting pattern. These approaches are briefly described in the following sections.

4.5.3. Pattern #5: Level lines of \mathcal{I}

Level lines can easily be deduced from \mathcal{I} by using the `mod` function of Matlab and thresholding the result. These level lines were serrated so that the image gradient along the direction perpendicular to the lines of greatest slope was not null. A typical example is shown in Figure 2-e. It was obtained with $\delta_x = -6$ pixels, $\delta_y = 0$ to be consistent with other displacement fields discussed below.

With this pattern, a problem is that the gray level distribution is flat between two consecutive lines, which is not a good point. Other patterns were therefore defined by inlaying various checkerboard images between these lines but the performance of DIC applied on this type of pattern was quite low,

so these patterns are not presented here.

4.5.4. Patterns #6 to #8: Poisson Image Editing on the displacement field modulated with Patterns #2 to #4

Principle. The second route considered here was to enhance the contrast by multiplying the displacement field in turn with the modulation function considered for Patterns #2 to #4. The modulation functions are f_{CKB_0} and f_{CIC} for Patterns #3 and #4, respectively. For Pattern #2, this is a function f_{spk_1} , which is easily deduced from the gray distribution I_{spk_1} for this pattern:

$$f_{spk_1} = (I_{spk_1} - \text{mean}(I_{spk_1})) / 255 \quad (16)$$

The product of the displacement field by this modulation function does not change the local gradient, which is therefore still given by the displacement alone. However, after applying PIE, it can be checked that the gradient of the resulting pattern is locally dominated by the gradient of the modulation function used to enhance the local contrast. It means that with this approach, the objective of aligning image gradient with the displacement field with can only be reached at a global level and not really at the local one, “global level” meaning for instance for a checkerboard a zone containing an integer number of periods.

Pattern #6, which is obtained by multiplying the displacement field by f_{spk_1} deduced from Pattern #2 (see Equation 16) and applying PIE, is depicted in Figure 2-f. Patterns #7 and #8 need special attention. They are discussed in the following two paragraphs.

Removing the fading effect for Pattern #8. For Pattern #8, the modulation of the gradient must be considered with care. Indeed, the mean value of f_{CIC} , which is the modulation function used in this case, is not null. Resolving the Poisson equation leads this non-null mean value to give rise to linear expressions of x and y in the gray level distribution of the resulting image. These expressions cause a fading of the checkerboard pattern to occur, and the contrast of the local texture is eventually low. This issue was overcome by directly removing this mean value from f_{CIC} , thus giving a new modulation function denoted by f'_{CIC} . The mean value of f_{CIC} was estimated piecewise to elaborate

f'_{CIC} , over the squares forming the large checkerboard for Pattern #4. This procedure significantly diminishes the contrast between bright and dark large squares for the pattern directly deduced from f'_{CIC} . Hence DIC directly applied on this type of pattern gives results which are worst than those obtained with f_{CIC} . On the contrary, when Poisson Image Editing is applied, this “fading effect” is removed and the contrast is enhanced. This eventually leads DIC to converge in any case, and obtained results are better than those got with Pattern #4, see Section 5 below.

Problem caused by $|g_x| = |g_y|$ for Patterns #7 and #8. For Patterns #7 and #8, a specific problem arises when $\left| \frac{\partial \mathcal{I}}{\partial x} \times f_{CKB_0} \right| = \left| \frac{\partial \mathcal{I}}{\partial y} \times f_{CKB_0} \right|$, where $|x|$ denotes the absolute value of x . The same phenomenon occurs for Pattern #8 when $\left| \frac{\partial \mathcal{I}}{\partial x} \times f'_{CIC} \right| = \left| \frac{\partial \mathcal{I}}{\partial y} \times f'_{CIC} \right|$. Indeed, in this case and considering that the origin is at the center of the hole, ($\delta_x = \delta_y = 0$), PIE provides a pattern with a texture oriented along the $\pm \frac{\pi}{4}$ directions in some zones. If these zones are too wide, image gradient is mainly oriented along one direction only over some subsets when applying DIC, which causes instabilities to occur along the direction perpendicular to this nearly unique gradient orientation. In other words, the displacement rendered by DIC is more prone to noise. The problem can be resolved by applying two types of corrections:

- Correction 1: searching for the corresponding zones, which is quite an easy task since they are characterized by an image gradient oriented along the $\frac{\pi}{4} + k\frac{\pi}{2}$ directions, k being an integer. These points are collected and the local orientation at these points is replaced by a constant angle close but different to $\frac{\pi}{4} + k\frac{\pi}{2}$. The new angle is indeed chosen to be equal to the value along the border of the region gathering the points where the displacement gradient belongs to one of the following sets: $(\frac{\pi}{4} + k\frac{\pi}{2} \pm \alpha), \alpha \neq 0$. It means that within this region, image gradient is constant and is not rigorously aligned with the displacement. Another consequence is to induce a discontinuity in the image gradient in the middle of each of these regions, with an amplitude equal to 2α . Figure 5 shows the different regions affected by this correction for three particular values for α , namely $\alpha = \frac{\pi}{24}, \frac{\pi}{12}$ and $\frac{\pi}{6}$. The location of the discontinuity affecting

image gradient is also visible at the middle of each region characterized by $\alpha = \pm \frac{\pi}{24}$. The effect of this correction is illustrated in Figure 6. It can be seen that both the systematic error and the random error decrease as α increases. The closeup views in Figure 6a shows one of the zones of the pattern where the errors are maximum. It is worth noting that in this zone, the pattern reduces to some parallel lines. The gradient is clearly oriented along a direction close (if not equal) to $\frac{\pi}{4}$, so the gray level derivative along the lines themselves is tiny, thus not sufficient to insure a robust determination of the displacement by DIC in this zone. The effect of an increasing value of α is illustrated in Figures 6d, 6g and 6j. A line breaking the regular arrangement of the pixels along the $-\frac{\pi}{4}$ progressively emerges, which provides an increasing robustness in the determination of the displacement by DIC. Slight welts are also visible. They are caused by the modulation of the image gradient by the displacement, which is accounted for in the construction of the pattern.

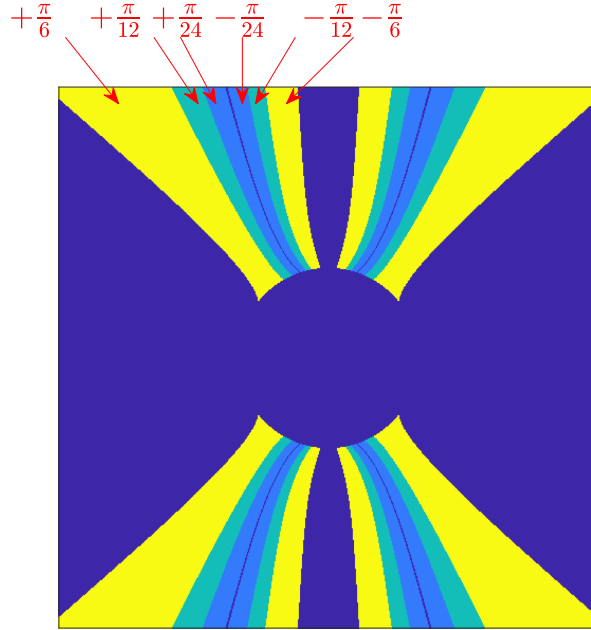


Figure 5: Three different angular portions for Correction 1. The different regions affected the correction are reported along with the corresponding value of α

- Correction 2: changing the arbitrary values of δ_x and δ_y . These quantities were defined in Section 4.5 above. They directly influence the local gradient orientation at any point since they

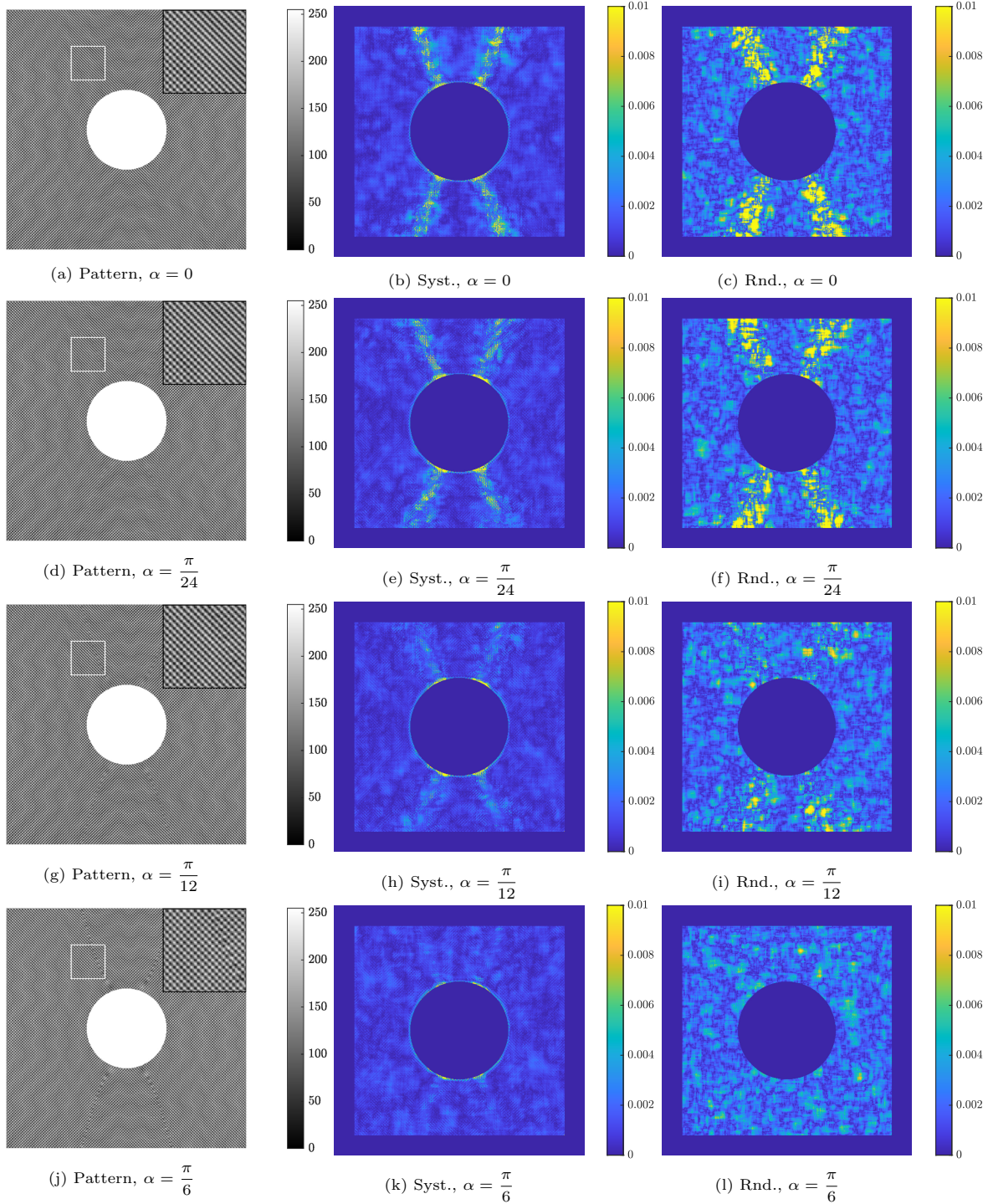


Figure 6: Effect of Correction 1. From the left to the right: pattern, systematic error and random error after correction of the gradient direction. From the top to the bottom: no correction ($\alpha = 0$), $\alpha = \frac{\pi}{24}$, $\frac{\pi}{12}$, $\frac{\pi}{6}$. On the left-hand side, the vertical rectangles bounded by white lines correspond to the zones where the closeup views are given.

determine the location of the origin of the displacement defined in Equation 14 above, and used to build up the pattern. Thus changing them is a convenient way to adjust the local image gradient orientation so that it is neither equal nor nearly equal to $\pm\frac{\pi}{4}$ at any point of the field under interest. It also means that the pattern itself also changes.

This remark underlines the fact that the pattern returned by PIE depends on the choice of the origin chosen to define the displacement which gives the global orientation of the image gradient. For real experiments however, a difference may exist between the real origin and the one which is used to define the pattern by using PIE, for instance if the specimen is sliding within the grips of the testing machine in the case of a tensile test. The question is to know to what extent this mismatch between these two origins (the assumed one used to render the pattern and the real one) impacts the quality of the results. The following simulation was performed to answer this question in a particular case. The value of (δ_x, δ_y) was first arbitrarily chosen to be equal to $(\delta_x, \delta_y) = (-6, 0)$ pixels and PIE was applied to render a pattern which was such that the image gradient orientation was neither equal nor nearly equal to $\pm\frac{\pi}{4}$ at any point of the zone around the hole. The displacement considered for deforming the pattern was then successively equal to $(-6, 0)$, $(-9, 0)$, $(-9, -3)$ and $(-12, -6)$ pixels. A mismatch is therefore deliberately introduced in the last three cases between the origin of the displacement field used to design the pattern and the origin of the displacement field actually deforming this pattern. The errors found in each case is reported in the diagram depicted in Figure 7. It can be seen that nearly the same result is obtained in each case. This is probably the consequence of the fact that changing the origin only slightly changes the orientation of the displacement field, the actual one being mainly dominated by the orientation of the loading itself since we deal here with a tensile test. Moreover, strain fields do not change when changing the location of the origin.

The RMSE obtained after applying Correction 1 with $\alpha = \frac{\pi}{6}$ is equal to $1.46 E - 03$. The RMSE after applying Correction 2 is equal to $1.23 E - 03$, which means that the latter is more efficient than the former. This result is likely due to the fact that in the first case, image gradient is not

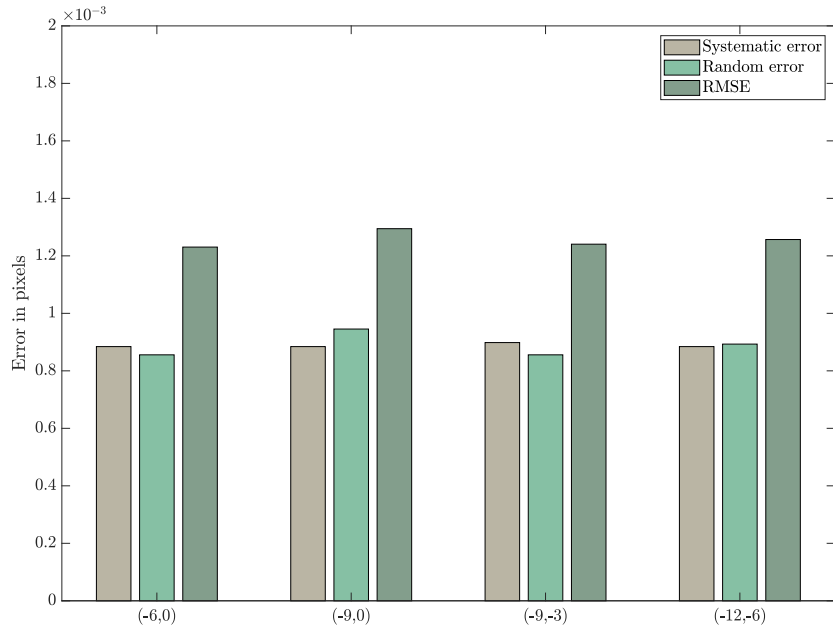


Figure 7: Errors for different locations of the origin.

rigorously collinear to the actual displacement over the zone impacted by the correction. In conclusion, $(\delta_x, \delta_y) = (-6, 0)$ pixels was used to render Patterns #5 et #8 discussed above and depicted in Figure 2. It is also worth mentioning that this type of correction shall be used only if the texture is oriented along one of the $\pm \frac{\pi}{4}$ directions, which was the case in the example discussed here. If this is not the case, no correction is applied.

5. Simulations

5.1. Procedure

The objective here is to illustrate with some examples to what extent using a pattern rendered by the procedures defined above improves the quality of the results obtained by DIC used with a classic speckle pattern. We consider the open-hole specimen defined in Section 4.5 above. The different patterns were considered in turn to define the reference image. These images were then deformed through the displacement field defined by Equations 13 and 14. Two values for the displacement of the left- and right-hand sides were chosen. The first value is ± 3 pixels. It corresponds to a case for which the displacement remains lower than the period of the checkerboard characterized by $p_0 = 6$ pixels. The second one is equal to ± 12 pixels. It is greater than p_0 but lower than p_1 characterizing the

large checkerboard since $p_1 = 48$ pixels. These two cases are referred to as the “small” and the “large” displacement cases, respectively.

All pairs of reference/deformed image were processed by DIC by using the settings described in Table 1. Noisy and noiseless images were considered in turn and the systematic and random errors as defined in Section 4.2 were estimated for each pattern, which enabled us to compare their performance.

5.2. Results

Figures 9 and 10 show the spatial distribution of the systematic error obtained for Patterns of types 1 and 2, respectively, and Figures 12 and 13 the distribution of the random error. They concern the small displacement case. The maps obtained in the large displacement case are gathered in Figures 11 and 14. The same colorbar is adopted for all the patterns in order to facilitate the comparison between the results. The systematic and random errors are given in Figure 15. The following comments can be drawn from these results:

- For small displacements, ranking the different patterns with respect to their RMSE leads to the following order when going from the best to the worst: #3, #8, #7, #4, #6, #2, #1, #5. The checkerboard (Pattern #3) is the best one, which confirms the conclusion given in [11, 23]. This is due to the fact that such a pattern exhibits a high image gradient [11], and that the pattern-induced bias is observed to be lower for periodic patterns like checkerboards than for classic random speckle patterns [19, 21]. The checkerboard pattern is closely followed by Pattern #8 ($RMSE = 1.23E - 03$ for the latter instead of $1.21E - 03$ for the former). The systematic error is smaller with Pattern #8. This is probably due to the fact that the orientation of the displacement is accounted for in the design of Pattern #8, which is not the case for Pattern #3. The random error is however lower for Pattern #3, which is logical since the image gradient is the highest possible in this case, but combining both the systematic and random errors gives the advantage to Pattern #3 with a small gap. The problem is that DIC does not converge with Pattern #3 for large displacements. A spectral method should be used instead [23] but including the results obtained in this case is out of the scope of the present paper. The reader is referred

to [23] for more details.

- For large displacements, DIC converged only for five patterns, and ranking them with respect to the RMSE leads to the following order: #8, #4, #6, #2, #1. By combining the results obtained in both the small and the large displacement cases, Pattern #8 can be considered as the best pattern for DIC of the eight examined here.
- Comparing Patterns #8 (RMSE= $1.23E - 03$ for small displacements and RMSE= $1.20E - 03$ for large displacements) and #4 (RMSE= $1.97E - 03$ and RMSE= $1.89E - 03$, respectively) shows that accounting for the displacement in the definition of the pattern leads to a decrease of the RMSE of 38% and 37% for the small and large displacement cases, respectively. The same remarks holds for Patterns #6 (RMSE= $2.47E - 03$ and RMSE= $2.83E - 03$, respectively) and #2 (RMSE= $3.14E - 03$ and RMSE= $3.55E - 03$, respectively), with a decrease of the RMSE of 21% and 20% for the small and large displacement cases, respectively. This bears witness to the fact that accounting for the displacement in the pattern design improves the metrological performance of DIC.
- Comparing Patterns #7 (RMSE = $1.34E - 03$) and #3 (RMSE = $1.22E - 03$) shows that on the contrary, applying PIE to the checkerboard alone does not improve the metrological performance for small displacements. Subtracting both patterns (not shown here) shows that the displacement accounted for in the design of Patterns #7 does not really impact it, which is not the case for Patterns #6 and #8 or #2 and #6. A possible reason is that the frequency of the checkerboard in Patterns #7 is too high to be influenced by PIE. The fact that the welts in Patterns #8 affects the border between the two types of checkerboards involved in Patterns #4 seems to show that PIE only affects frequencies lower than the frequency of the checkerboard alone.
- As mentioned above, DIC converged for only five patterns (#1, #2, #4, #6 and #8) in the case of large displacements. The reasons are as follows. Pattern #3 being periodic, DIC converges

to a local minimum in the large displacement case. For Pattern #5, DIC does not converge to the solution because there is no gradient between the level lines in some zones. Tightening these lines is not really possible, the distance being already quite small in some regions of this pattern, see Figure 2-e. Attempts to inlay local contrast in these flat zones by adding a checkerboard of various periods did not improve the results. DIC does not converge for Pattern #7 because the periodicity of the small checkerboard is not sufficiently modified by the modulation by the displacement.

- Comparing the results obtained with Patterns #1 and #2 illustrates the improvement brought about by controlling the shape of the random speckles as proposed in [10]. Observing the spatial distribution for the systematic error in Figures 9a and 9b, and for the random error in Figures 12a and 12b, shows that the systematic error diminishes when going from Pattern #1 to #2, while the random error is slightly lower for Pattern #1.
- The total error is about 7 times greater for Pattern #1 than for Pattern #8 ($9.01E - 03$ and $1.23E - 03$, respectively). As a general remark, this illustrates the benefit of using optimized patterns in DIC instead of classic random ones.

5.3. Numerical evidence of the influence of image gradient orientation on the quality of the results obtained with DIC

We propose here to illustrate and quantify the effect of collinearity between image gradient and displacement field by reconsidering the best pattern above, namely Pattern #8. Indeed, special attention was paid to perfectly aligning the image gradient with the displacement field given by Equations 13 and 14. The idea here is to consider a pattern, which is expected to be the worst case if the objective is to align both fields. Indeed, we considered an image, for which the gradients are perpendicular instead of collinear to the displacement field. For this, the normalized displacement given by Equation 15 was rotated at any point by $\frac{\pi}{2}$. This new normalized displacement was multiplied by the modulating function of Pattern #4, and the result was integrated by applying PIE, which gives Pattern #8bis. Both Patterns #8 and #8bis are depicted in Figure 8. The RMSE value for Pattern #8 is equal to

$1.23 E - 03$ pixel while its counterpart for Pattern #8bis is equal to $1.49 E - 03$ pixel, which is 21% higher. Interestingly, the systematic error is nearly the same for both patterns. Only the random pattern increases when considering Pattern #8bis instead of Pattern #8. This result supports the rationale that the image gradient should be collinear to the displacement, and quantifies the benefit of this approach in this particular case. As a final remark, the reader might be surprised to see that the RMSE value for Pattern #4 ($RMSE = 1.97E - 03$) does not lie between the RMSE values of Patterns #8 and #8bis. The reason is the local average of the gray level distribution is removed for Patterns #8 and #8bis, as explained in Section 4.5.4, which is not the case for Pattern #4. Applying the same averaging procedure to Pattern #4 causes DIC not to converge in the case of large displacements, so the corresponding results are not reported here.

6. Experiments

The objective here is to observe the quality of the displacement and strain fields obtained experimentally when using some of the patterns discussed above. With experiments, the ground truth remains however unknown apart from the case of solid-rigid body motions, for which it can only be said that the strain field is expected to be null. Discussing both the systematic and the random errors in this case, as we did above with synthetic data, is therefore not really possible. Another concern is the possibility of depositing in some way the desired patterns. No technical solution was available in the laboratory to print patterns in which intermediate gray levels should be thoroughly mastered. This is mainly the case for patterns of type 2. As a consequence, we only focused our investigations in the following on comparing the effect of sensor noise propagation to the displacement and strain maps. Two cases were considered: the case of a completely random pattern as Pattern #1, and Pattern #4, with two checkerboards featuring each a different scale. The first pattern was obtained by merely spray painting the specimen in white with a uniform layer, and then in black with droplets randomly distributed. Pattern #4 was deposited by first spray painting the specimen uniformly in white and then by using a laser engraver fed by a file containing the geometric description of this pattern. Full details concerning the performance obtained with the patterns obtained with this laser

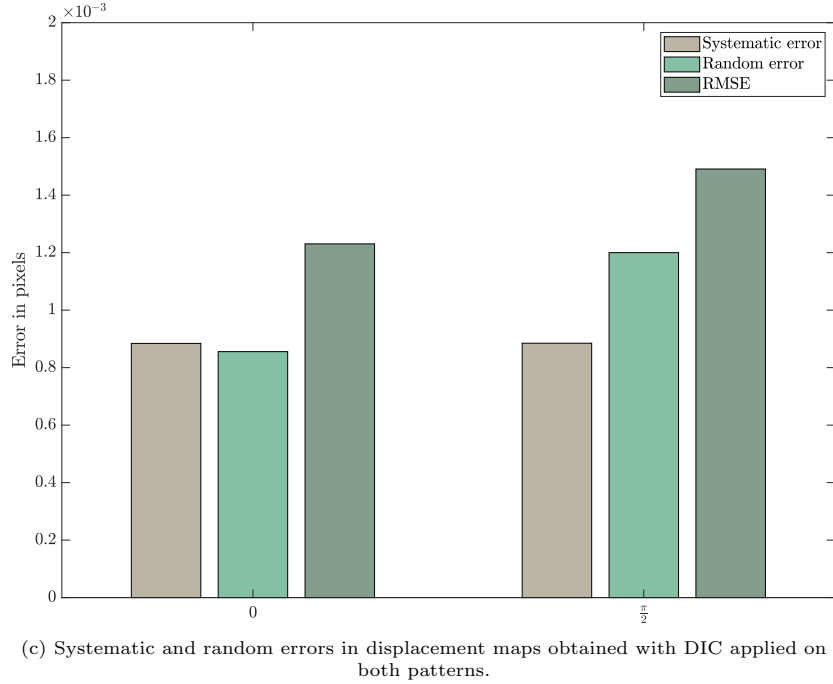
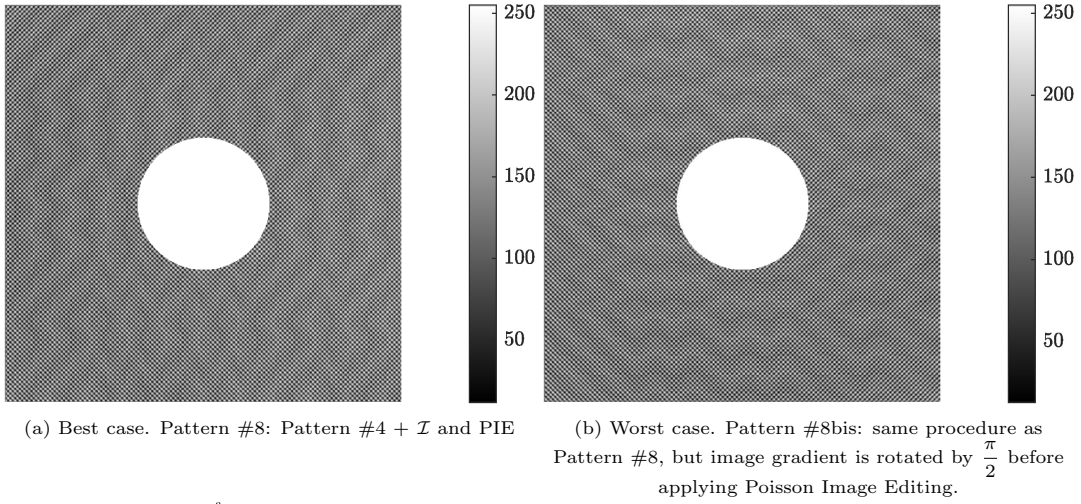


Figure 8: Pattern #8 and Pattern #8bis. Pattern #8bis is obtained in a way similar to Pattern #8 but image gradient is rotated by $\frac{\pi}{2}$ before applying Poisson Image Editing.

engraver are available in [55]. We considered two open-hole specimens (one for each type of pattern) made in aluminum. Their dimensions were $200 \times 50 \times 1.5 \text{ mm}^3$. The diameter of the hole was equal to 15 mm. Both specimens were subjected to a tensile test performed with a Zwick-Roll tensile machine. The camera used to capture the images was a Prosilica GT 6600 featuring a CCD sensor of size $6576 \times 4384 \simeq 28.8\text{E}+06$ pixels, with a gray depth equal to 8 bits. The lens was a Nikkor Micro

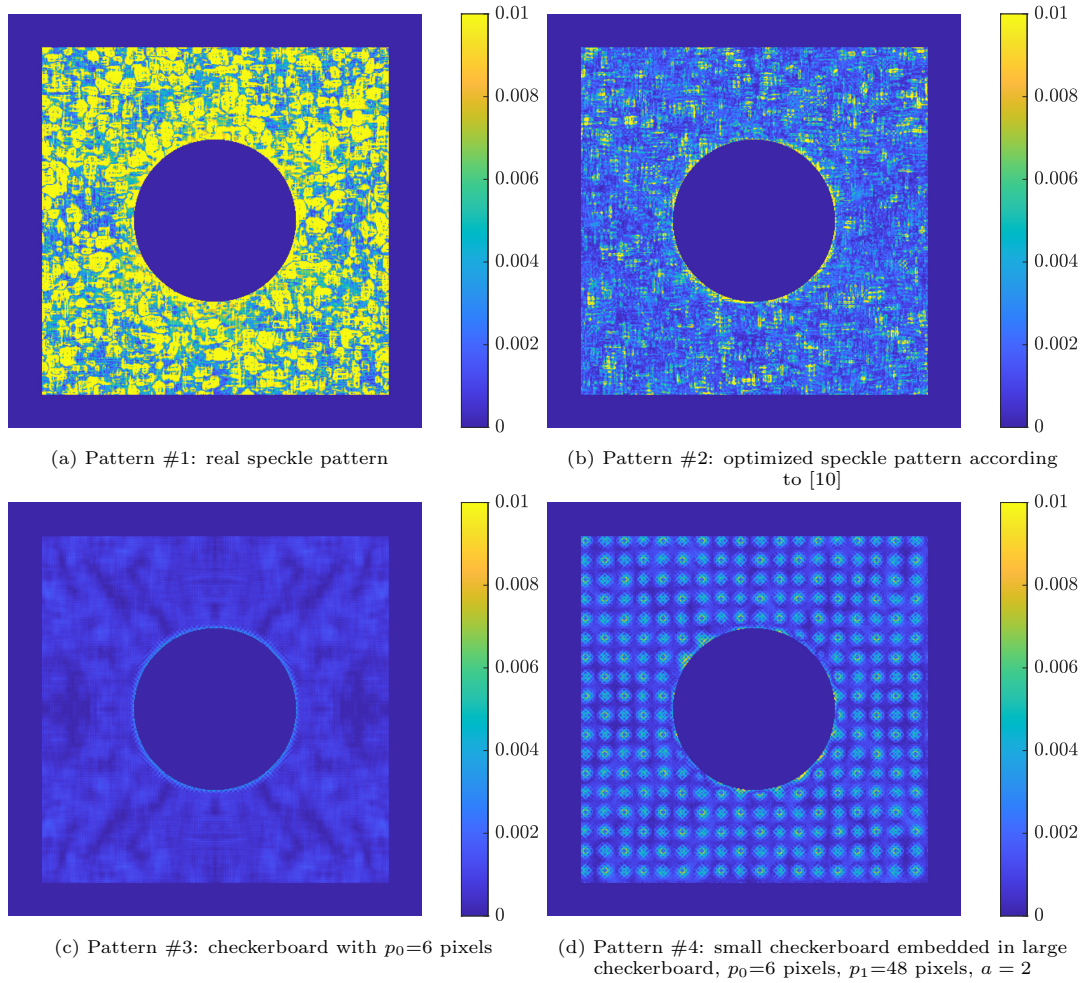


Figure 9: Distribution of the systematic error for the four patterns of type 1. Small displacement.

200 F4 AF-D. Two LED light sources were placed symmetrically along the left- and right-hand sides of the specimen under test. The camera was fixed in such a way that the border of the specimen was aligned with the rows of pixels of the camera. The displacement-controlled loading rate was equal to 1 mm/mn. The shutter time and the aperture of the lens were adjusted in such a way that the best contrast was obtained in the images.

Figure 17 shows the typical displacement fields measured during the test for a force equal to 3000 N. Similar aspects and values for the displacement fields are obtained with these two patterns.

100 pairs of images were recorded in each case and the 100 corresponding displacement fields were then extracted with DIC. The standard deviation was calculated pixelwise for each component

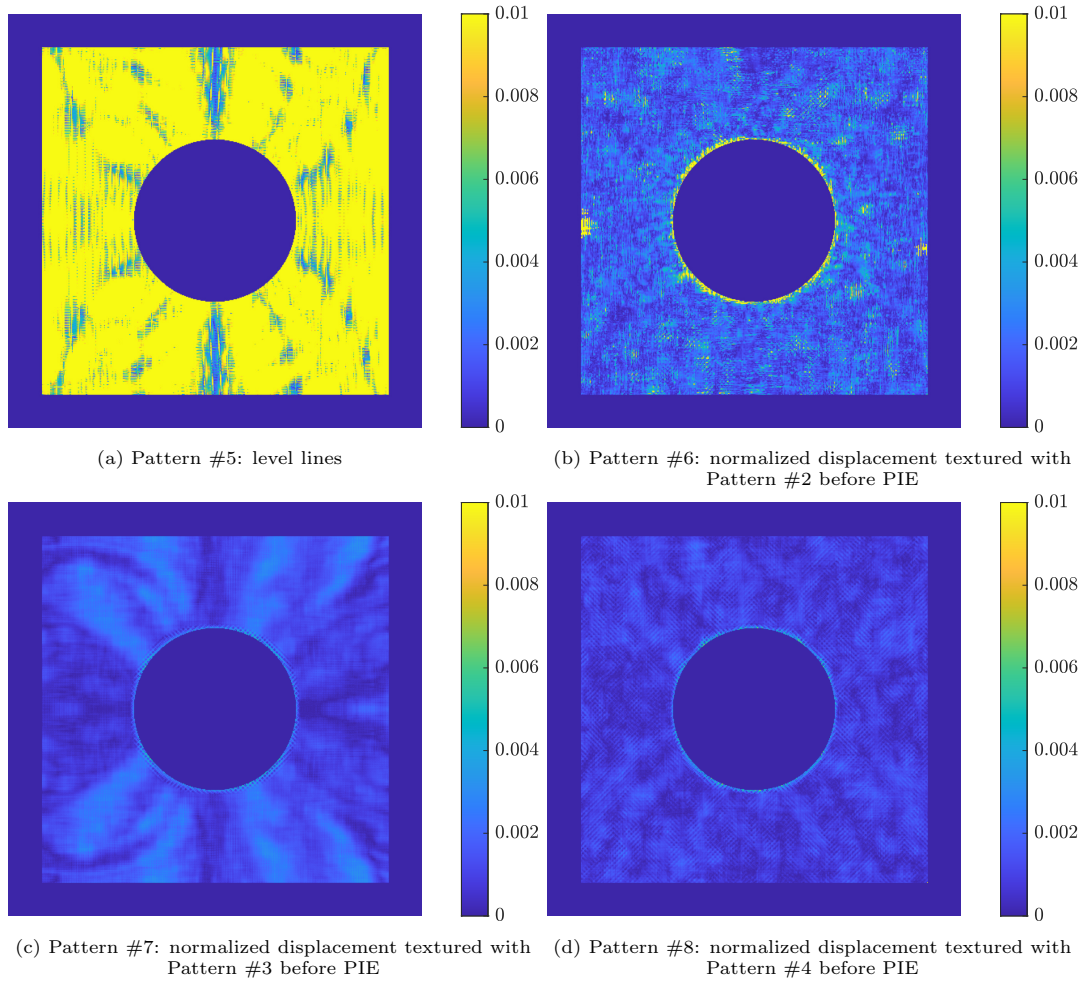


Figure 10: Distribution of the systematic error for the four patterns of type 2. Small displacement.

of the 100 displacement maps. The mean value of the x - and y -displacement was first subtracted from respectively the u_x and the u_y displacement distributions in order to get rid of potential micro-vibrations (at least those causing small translations to occur), as in similar studies dealing with noise estimation in displacement maps, [18, 55] for instance. It can be observed in Figure 19d that these maps are not uniform. The low-frequency spatial fluctuations of the standard deviation are due to the non-uniformity of the light over the front face of the specimen. Another remark is that the standard deviation of the noise is significantly greater for the classic random pattern than for Pattern #4, which is in agreement with what was predicted in the previous section. This is confirmed by considering the histograms of these four standard distributions, which are plotted in Figure 18 with the same

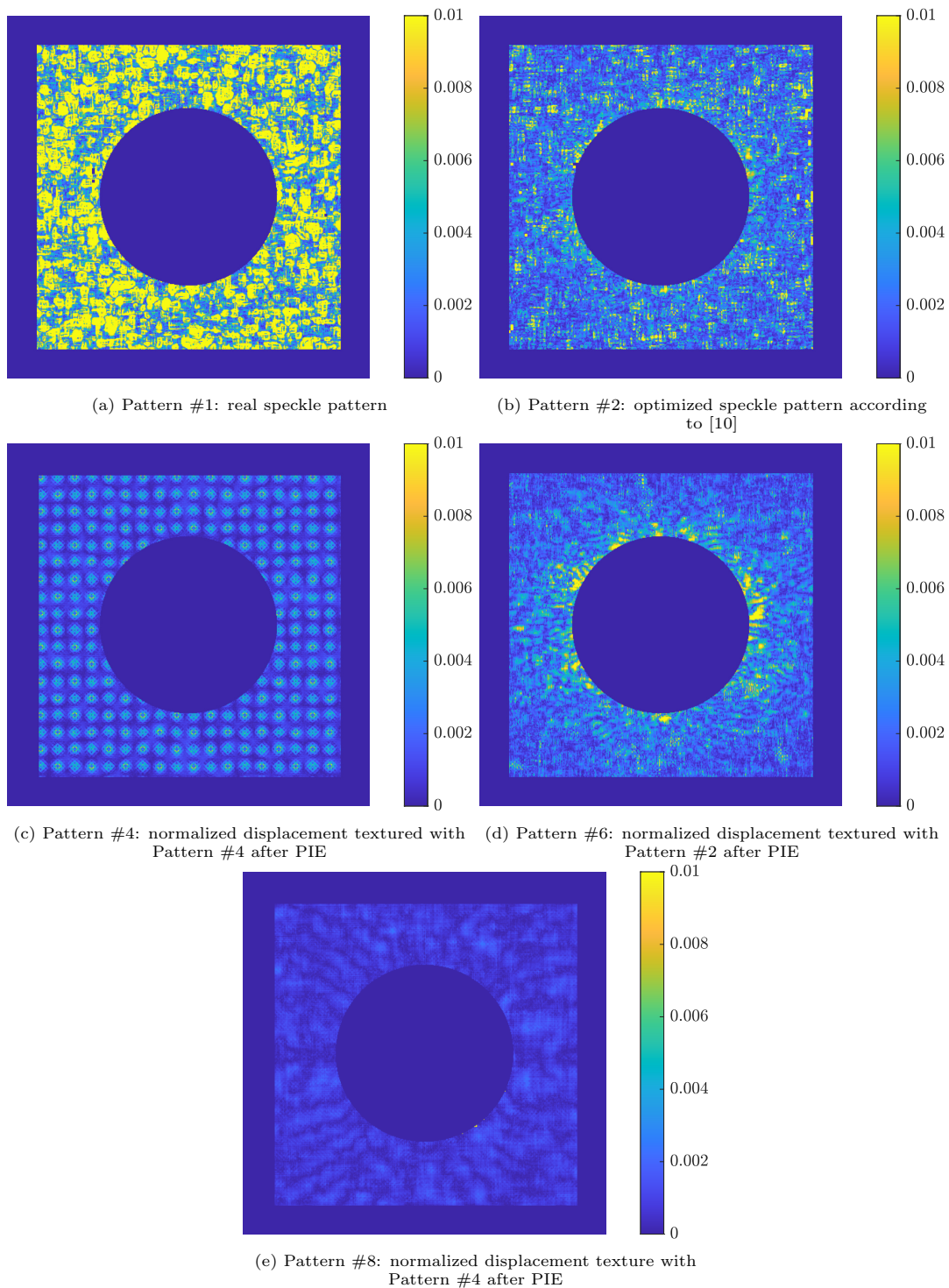


Figure 11: Distribution of the systematic error for the patterns of type 1 or 2 converging in the case of large displacement.

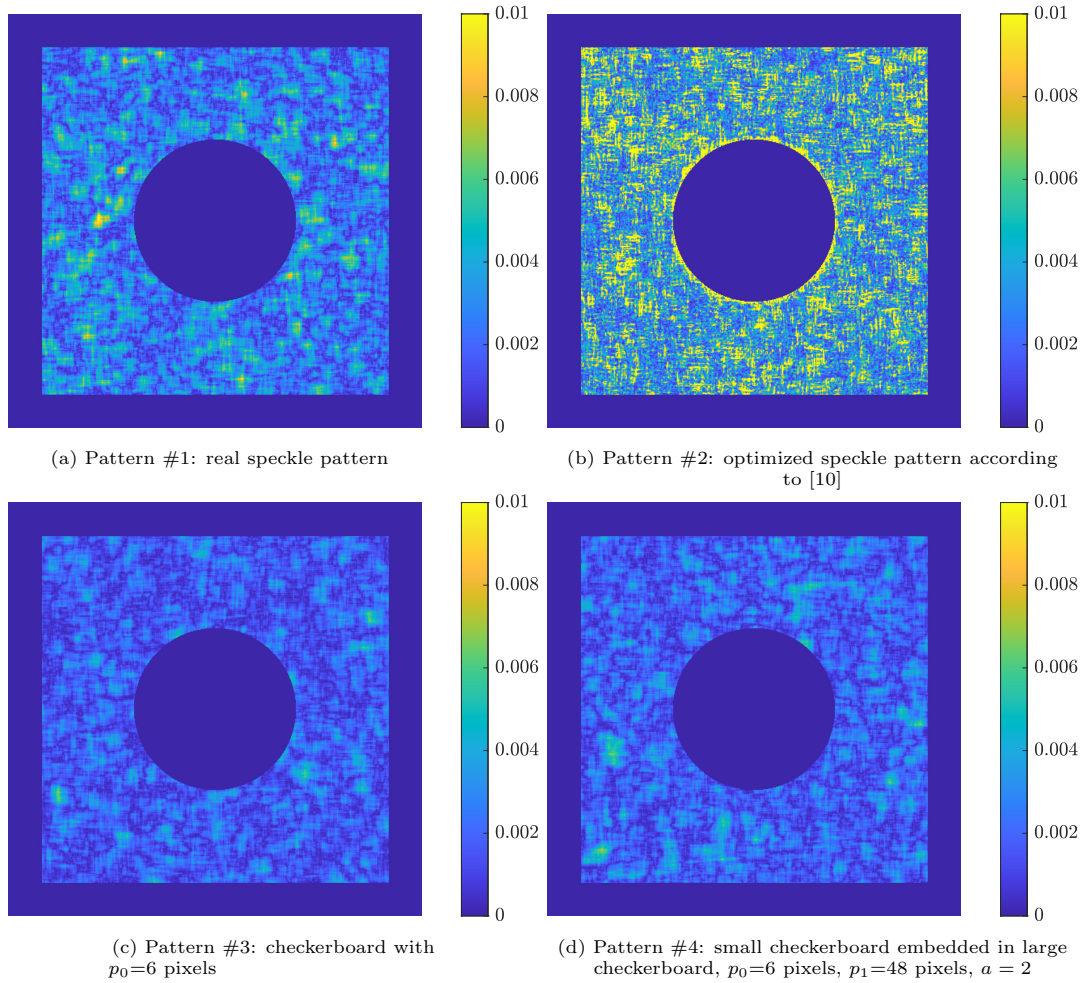


Figure 12: Distribution of the random error for the four patterns of type 1. Small displacement.

scale along the horizontal axis. These histograms are not symmetric and somewhat irregular, which is probably due to the fact that the parasitic micromovements were not perfectly removed from the displacement fields. The noise level is also slightly higher along the loading direction (namely x -direction) as in similar studies, [18, 55] for instance. The most striking remarks are *i*- the fact that the histograms are narrower for Pattern #4 than for the classic random pattern, which is certainly due to the more regular aspect of Pattern #4, and *ii*- that they are shifted to the left in the second case, which means that the noise level is lower. This is confirmed by comparing the global standard deviation reported in the caption of the four sub-figures. The noise is indeed nearly twice lower with the second pattern. The ratio is greater than that observed with the simulations, see the random errors

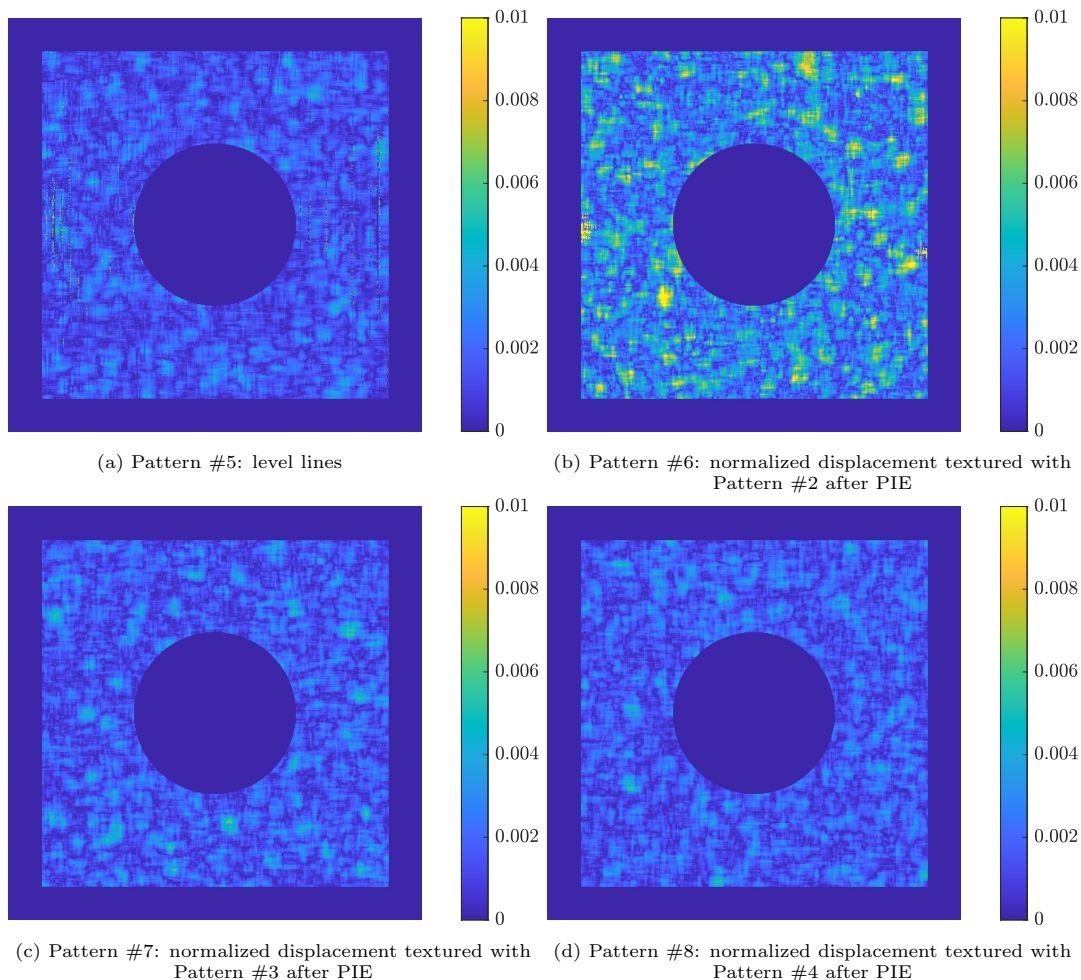


Figure 13: Distribution of the random error for the four patterns of type 2. Small displacement. DIC did not converge at some points, see subfigure (a). The corresponding points are considered as outliers in the calculation of the systematic and random errors.

for Pattern #1 and #4 in Figures 15a and 15b which are 40 % and 60% for Pattern #1 for small and large displacements, respectively, but the random speckle is not the same for the simulations and for experiments. Both the numerical and the experimental results confirm however that Pattern #4 leads to better performance than Pattern #1 in terms of level of the random errors.

7. Conclusion

The quality of the displacement and strain fields obtained by DIC with various patterns were compared in this study. We first mainly focused on the influence of the collinearity between the displacement field and the image gradient of the pattern. Synthetic patterns with maximum and

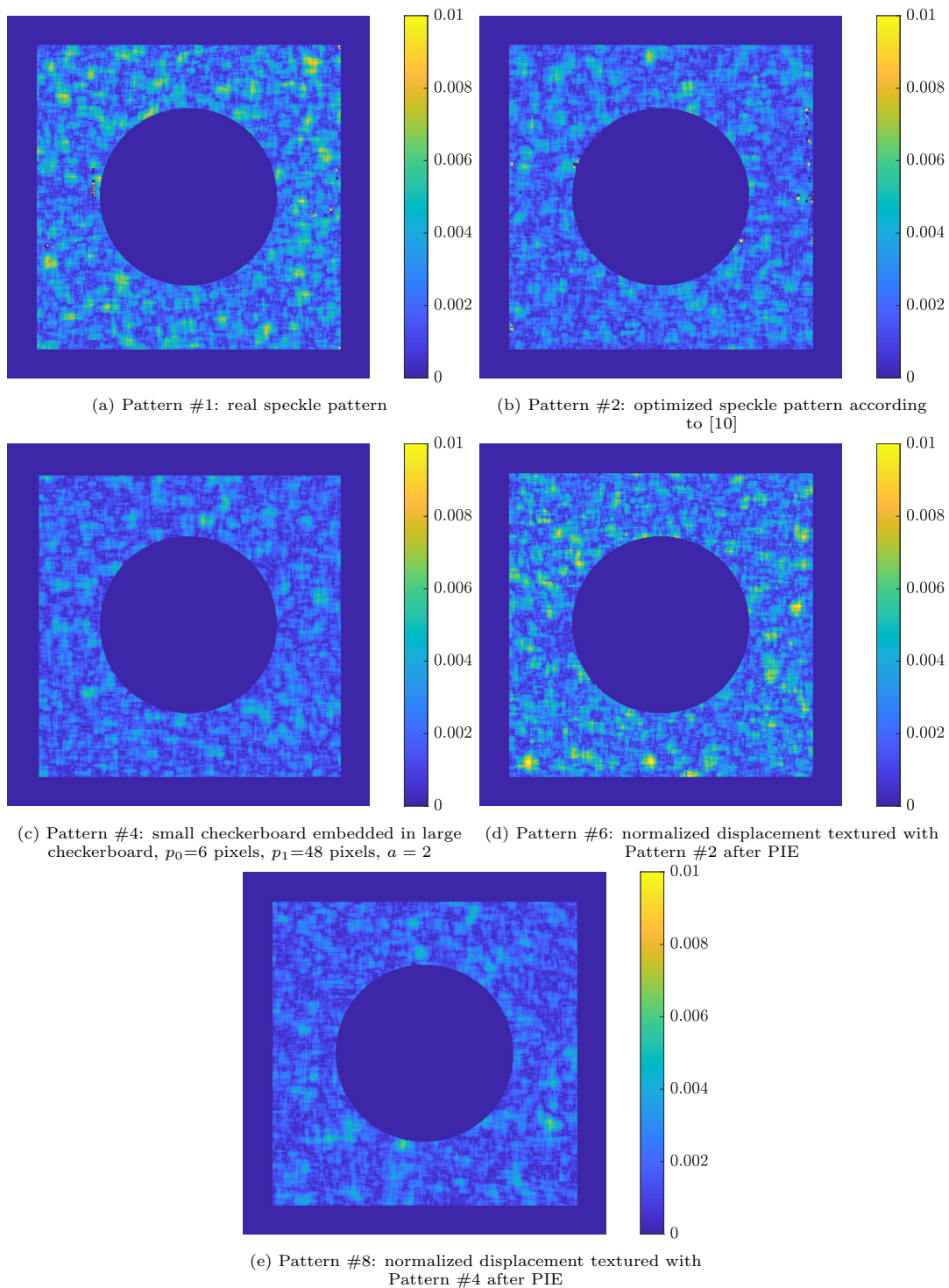


Figure 14: Distribution of the random error for the patterns of type 1 or 2 converging in the case of large displacement.

minimum degrees of collinearity estimated globally were obtained by Poisson Image Editing (PIE). The displacement was modulated by different textures to increase the image gradient, and make DIC utilisable with patterns provided by PIE. The conclusion is that the higher this global collinearity, the lower the error. The improvement brought about by adjusting at best this collinearity has been found to be equal to 21% compared to the worst case. Future work should consider other particular cases of displacement fields to consolidate this first result. Another problem is to have a printing device able to deposit such patterns on the surface of specimens to be tested, the challenge being here to precisely control the local gray level gradient.

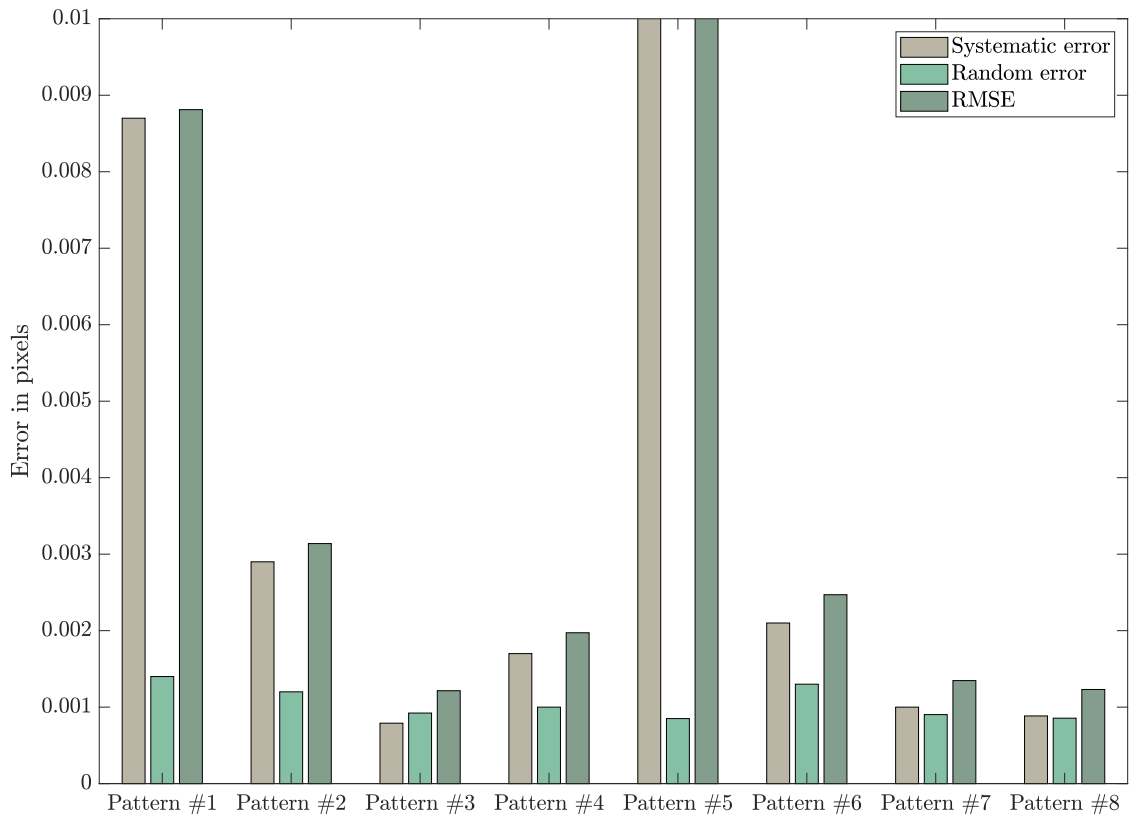
As a general remark, the best pattern for measuring displacement fields is a mere checkerboard, which has been confirmed once again in the present study in case of displacement with an amplitude lower than the period of the checkerboard. DIC cannot measure displacement greater in amplitude than the period of such a pattern, but this hurdle can easily be overcome by switching the minimization of the optical residual from the spatial to the frequency domain, and using a spectral method to find the solution, as documented in recent papers. We also showed in this study that it was possible to “adapt” the checkerboard pattern to DIC by associating two checkerboards, each of them having a different period. In this case, DIC converges to the solution if the amplitude of the displacement is lower than the highest of the two periods, and the metrological performance is close to the one obtained with a simple checkerboard processed with DIC for a displacement lower in amplitude than its period.

Acknowledgment

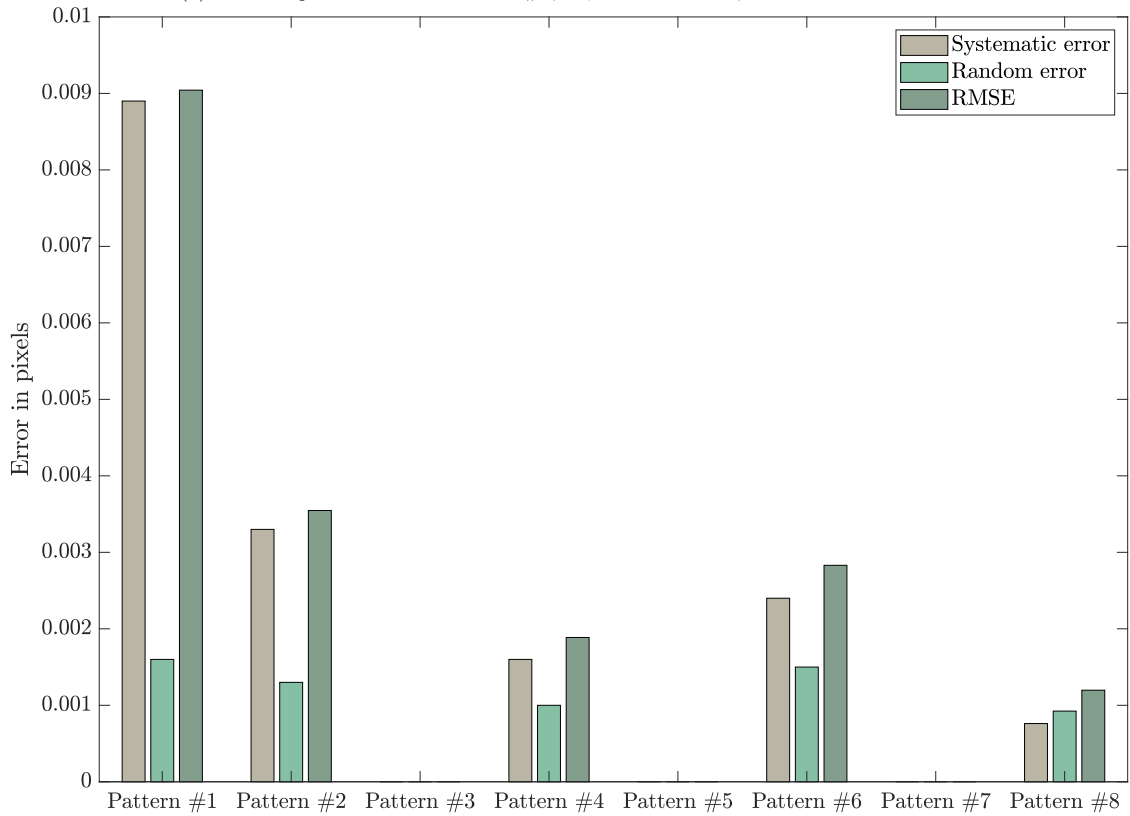
The authors acknowledge support from the ANR Grant ANR-18-CE08-0028-01. This work has also been sponsored by the French government research program “Investissements d’Avenir” through the IDEX-ISITE initiative 16-IDEX-0001 (CAP 20-25) and the IMobS3 Laboratory of Excellence (ANR-10-LABX-16-01). Dr. Rian Seghir is gratefully acknowledged for providing the Matlab program used to render Pattern #2.

Ethics declarations/Conflict of Interest

The authors declare that they have no conflict of interest.

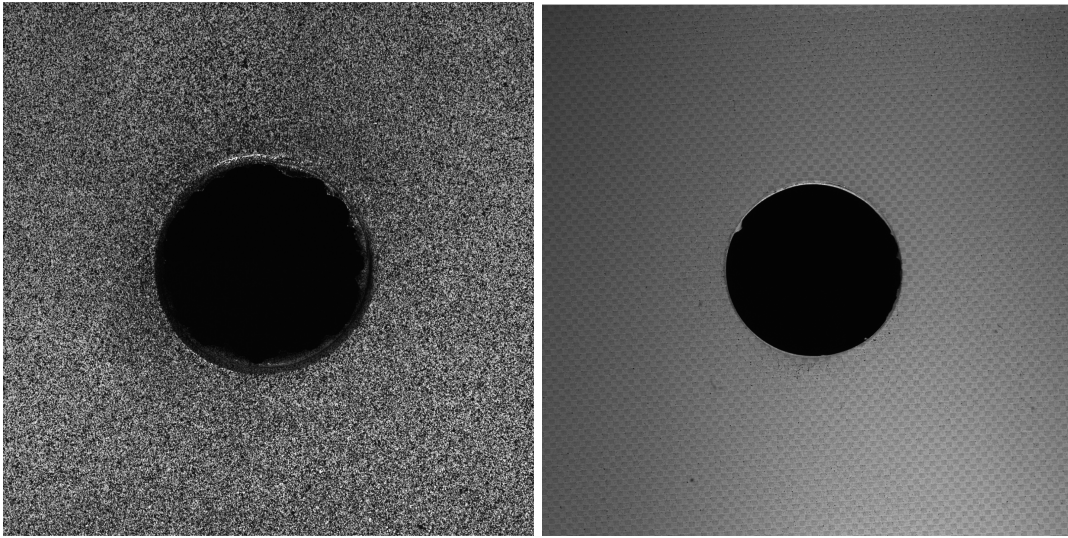


(a) Small displacement. For Pattern #5, $M_s = 22.20E - 03$, $RMSE = 22.22E - 03$



(b) Large displacement

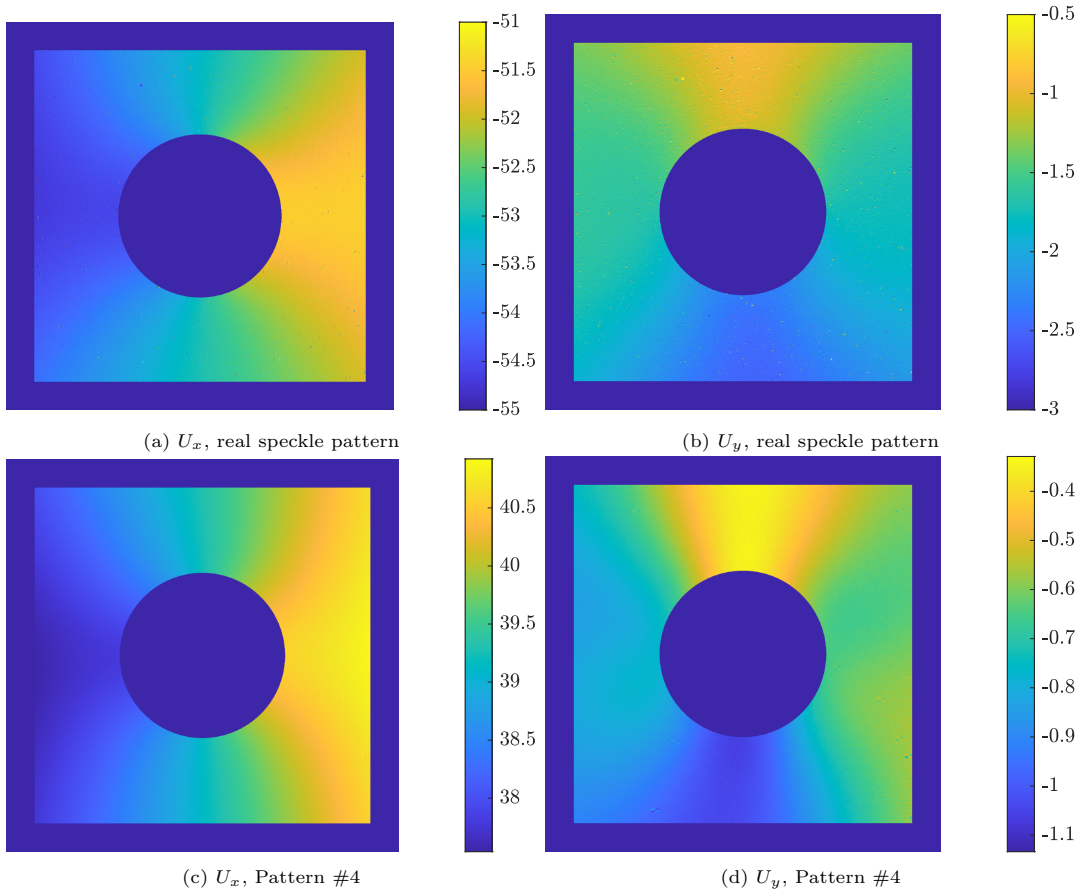
Figure 15: Error observed for the different patterns.



(a) Random speckle pattern

(b) Pattern #4

Figure 16: Closeup view of the patterns deposited on the two tested specimens.



(a) U_x , real speckle pattern

(b) U_y , real speckle pattern

(c) U_x , Pattern #4

(d) U_y , Pattern #4

Figure 17: Displacement field obtained with a classic random speckle (top) and with Pattern #4 (bottom).

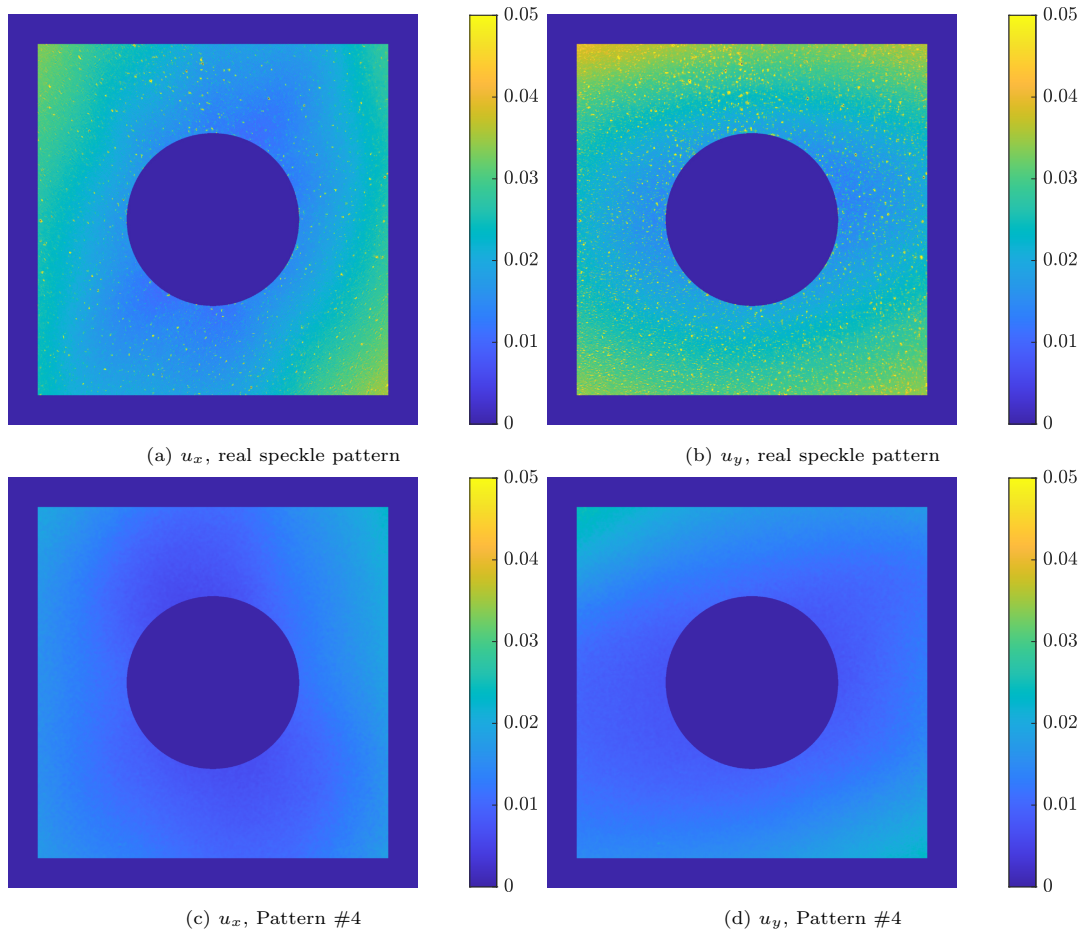


Figure 18: Standard deviation of the displacement retrieved at each pixel of the displacement maps for the classic random speckle (top) and for Pattern #4 (bottom).

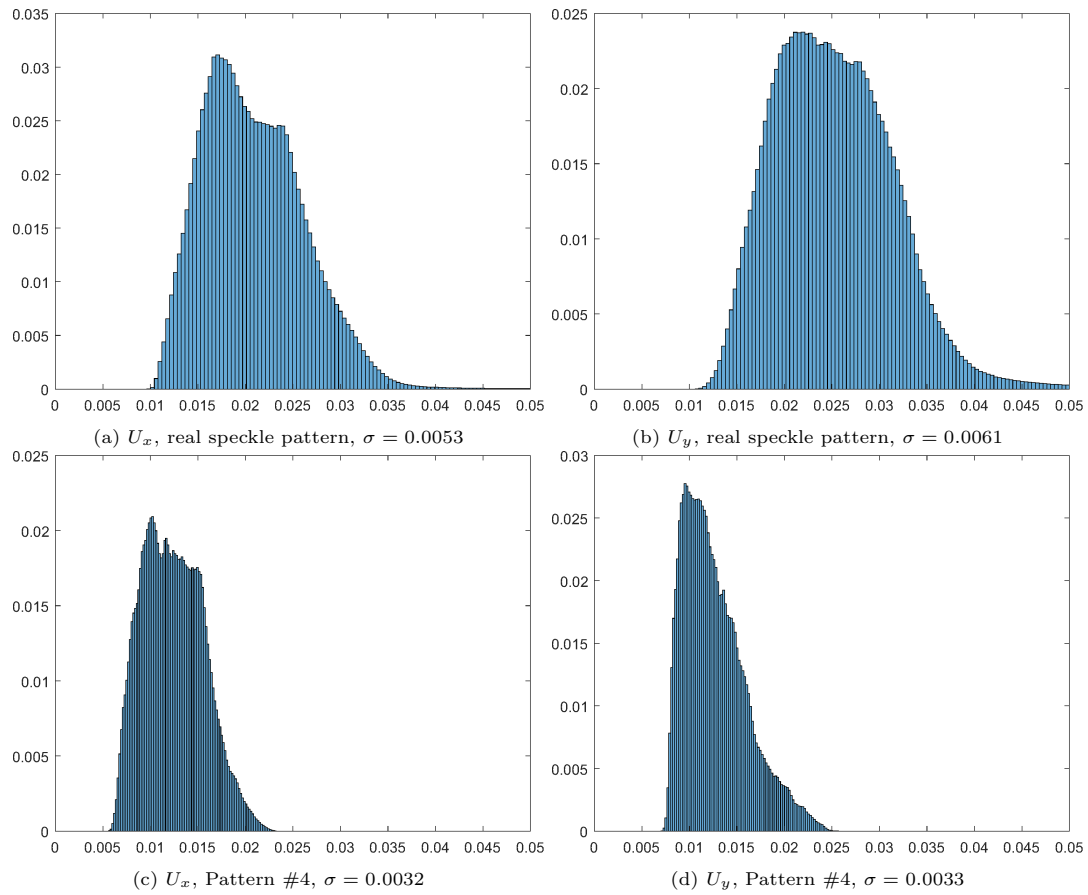


Figure 19: Histogram of the standard deviation of the displacement retrieved at each pixel of the displacement maps for the classic random speckle (top) and for Pattern #4 (bottom).

References

- [1] Y. Su, Q. Zhang, X. Xu, and Z. Gao. Quality assessment of speckle patterns for DIC by consideration of both systematic errors and random errors Reference image Deformed image. *Optics and Lasers in Engineering*, 86:132–142, 2016.
- [2] D. Lecompte, A. Smits, S. Bossuyt, H. Sol, J. Vantomme, D. Van Hemelrijck, and A.M. Habraken. Quality assessment of speckle patterns for digital image correlation. *Optics and Lasers in Engineering*, 44(11):1132–1145, 2006.
- [3] G. Crammond, S. Boyd, and J. Dulieu-Barton. Speckle pattern quality assessment for digital image correlation. *Optics and Lasers in Engineering*, 51:1368–1378, 2013.
- [4] P. Reu. All about speckles: Aliasing. *Experimental Techniques*, 38(5):1–3, 2014.
- [5] J. Park, S. Yoon, T. Kwon, and K. Park. Assessment of speckle-pattern quality in digital image correlation based on gray intensity and speckle morphology. *Optics and Lasers in Engineering*, 91:62 – 72, 2017.
- [6] T. Hua, H. Xie, S. Wang, Z. Hu, P. Chen, and Q. Zhang. Evaluation of the quality of a speckle pattern in the digital image correlation method by mean subset fluctuation. *Optics and Laser Technology*, 43(1):9–13, 2011.
- [7] X. Liu, R. Li, H. Zhao, T. Cheng, G. Cui, Q. Tan, and G. Meng. Quality assessment of speckle patterns for digital image correlation by Shannon entropy. *Optik*, 126(23):4206–4211, 2015.
- [8] B. Pan, H. Xie, Z. Wang, K. Qian, and Z. Wang. Study on subset size selection in digital image correlation for speckle patterns. *Optics Express*, 16(10):7037, 2008.
- [9] B. Pan, Z. Lu, and H. Xie. Mean intensity gradient: An effective global parameter for quality assessment of the speckle patterns used in digital image correlation. *Optics and Lasers in Engineering*, 48(4):469–477, 2010.

- [10] S. Bossuyt. Optimized patterns for digital image correlation. In *Conference Proceedings of the Society for Experimental Mechanics Series*, volume 3, pages 239–248, 2013.
- [11] G.F. Bomarito, J.D. Hochhalter, T.J. Rugglesb, and A.H. Cannon. Increasing accuracy and precision of digital image correlation through pattern optimization. *Optics and Lasers in Engineering*, 91(April):73–85, 2017.
- [12] H.W. Schreier, J.R. Braasch, and M.A. Sutton. Systematic errors in digital image correlation caused by intensity interpolation. *Library*, 39(November):2915–2921, 2000.
- [13] G.F. Bomarito, J.D. Hochhalter, and T.J. Ruggles. Development of optimal multiscale patterns for digital image correlation via local grayscale variation. *Experimental Mechanics*, 58(7):1169–1180, 2018.
- [14] J. Song, J. Yang, F. Liu, and K. Lu. Quality assessment of laser speckle patterns for digital image correlation by a multi-factor fusion index. *Optics and Lasers in Engineering*, 124:105822, 2020.
- [15] Y.L. Dong and B. Pan. A review of speckle pattern fabrication and assessment for digital image correlation. *Experimental Mechanics*, 57(8):1161–1181, 2017.
- [16] M. Mathew, B. Wisner, S. Ridwan, M. McCarthy, I. Bartoli, and A. Kontsos. A bio-inspired frequency-based approach for tailorable and scalable speckle pattern generation. *Experimental Mechanics*, 60:1103–1117, 2020.
- [17] R. Fouque, R. Bouclier, J. C. Passieux, and J.-N. Périé. Fractal pattern for multiscale digital image correlation. *Experimental Mechanics*, 61(3):483–497, 2021.
- [18] M. Grédiac, B. Blaysat, and F. Sur. Extracting displacement and strain fields from checkerboard images with the Localized Spectrum Analysis. *Experimental Mechanics*, 59(2):207–218, 2019.
- [19] S.S. Fayad, D.T., Seidl, and P.L. Reu. Spatial DIC errors due to Pattern-Induced Bias and grey level discretization. *Experimental Mechanics*, 60(2):249–263, 2020.

- [20] R.B. Lehoucq, P.L. Reu, and D.Z. Turner. The effect of the ill-posed problem on quantitative error assessment in digital image correlation. *Experimental Mechanics*, 61(3):609–621, 2021.
- [21] F. Sur, B. Blaysat, and M. Grédiac. On biases in displacement estimation for image registration, with a focus on photomechanics. *Journal of Mathematical Imaging and Vision*, 63:777–806, 2021.
- [22] M. Grédiac, B. Blaysat, and F. Sur. A Critical Comparison of Some Metrological Parameters Characterizing Local Digital Image Correlation and Grid Method. *Experimental Mechanics*, 57(6):871–903, 2017.
- [23] M. Grédiac, B. Blaysat, and F. Sur. On the Optimal Pattern for Displacement Field Measurement: Random Speckle and DIC, or Checkerboard and LSA? *Experimental Mechanics*, 60(4):509–534, 2020.
- [24] S Roux, J. Réthoré, and F. Hild. Digital image correlation and fracture: an advanced technique for estimating stress intensity factors of 2D and 3D cracks. *Journal of Physics D: Applied Physics*, 42:214004, 2009.
- [25] G. Rebergue, B. Blaysat, H. Chanal, and E. Duc. Advanced DIC for accurate part deflection measurement in a machining environment. *Journal of Manufacturing Processes*, 33:10–23, 2018.
- [26] G. Zi and T. Belytschko. New crack-tip elements for XFEM and applications to cohesive cracks. *International Journal for Numerical Methods in Engineering*, 57(15):2221–2240, 2003.
- [27] Y.Q. Wang, M.A. Sutton, H.A. Bruck, and H.W. Schreier. Quantitative error assessment in pattern matching: Effects of intensity pattern noise, interpolation, strain and image contrast on motion measurements. *Strain*, 45(2):160–178, 2009.
- [28] R. Fattal, D. Lischinski, and M. Werman. Gradient domain high dynamic range compression. *ACM Transactions on Graphics*, 21(3):249–256, 2002.
- [29] P. Pérez, M. Gangnet, and A. Blake. Poisson image editing. *ACM SIGGRAPH 2003 Papers, SIGGRAPH '03*, 6:313–318, 2003.

- [30] T. Georgiev. Covariant derivatives and vision. *Lecture Notes in Computer Science (including subseries Lecture Notes in Artificial Intelligence and Lecture Notes in Bioinformatics)*, 3954 LNCS(May 2006):56–69, 2006.
- [31] J. Shen, X. Jin, C. Zhou, and C. Wang. Gradient based image completion by solving. *Computers & Graphics*, 31(1):119–126, 2007.
- [32] J. M. Di Martino, G. Facciolo, and E. Meinhardt-Llopis. Poisson Image Editing. *Image Processing On Line*, 6:300–325, 2016.
- [33] A. Levin, A. Zomet, S. Pelegl, and Y. Weiss. Seamless image stitching in the gradient domain. *Lecture Notes in Computer Science (including subseries Lecture Notes in Artificial Intelligence and Lecture Notes in Bioinformatics)*, 3024(February):377–389, 2004.
- [34] J.M. Morel, A.B. Petro, and C. Sbert. Fourier implementation of Poisson image editing. *Pattern Recognition Letters*, 33(3):342–348, feb 2012.
- [35] F. Caforio and S. Imperiale. A high-order spectral element fast fourier transform for the poisson equation. *SIAM Journal on Scientific Computing*, 41(5):A2747–A2771, 2019.
- [36] B. Blaysat, J. Neggers, M. Grédiac, and F. Sur. Towards criteria characterizing the metrological performance of full-field measurement techniques. application to the comparison between local and global versions of DIC. *Experimental Mechanics*, 60(3):393–407, 2020.
- [37] International Digital Image Correlation Society, Jones, E.M.C. and Iadicola, M.A. (Eds). A good practices guide for Digital Image Correlation. <https://doi.org/10.32720/idics/gpg.ed1>, 2018. Online.
- [38] H.W. Schreier, M.A. Sutton, and A. Michael. Systematic errors in digital image correlation due to undermatched subset shape functions. *Experimental Mechanics*, 42(3):303–310, 2002.

- [39] M. Grédiac, B. Blaysat, and F. Sur. A critical comparison of some metrological parameters characterizing local digital image correlation and grid method. *Experimental Mechanics*, 57(6):871–903, 2017.
- [40] A. Savitzky and M.J.E. Golay. Smoothing and differentiation of data by simplified least-squares procedures. *Analytical Chemistry*, 36(3):1627–1639, 1964.
- [41] A. Foi, M. Trimeche, V. Katkovnik, and K. Egiazarian. Practical Poissonian-Gaussian noise modeling and fitting for single-image raw-data. *IEEE Transactions on Image Processing*, 17(10):1737–1754, 2008.
- [42] M. Grédiac and F. Sur. Effect of sensor noise on the resolution and spatial resolution of the displacement and strain maps obtained with the grid method. *Strain*, 50(1):1–27, 2014. Paper invited for the 50th anniversary of the journal. Wiley.
- [43] P. L. Reu, B. Blaysat, E. Andó, K. Bhattacharya, C. Couture, V. Couty, D. Deb, S. S. Fayad, M. A. Iadicola, S. Jaminion, M. Klein, A. K. Landauer, P. Lava, M. Liu, L. K. Luan, S. N. Olufsen, J. Réthoré, E. Roubin, D. T. Seidl, T. Siebert, O. Stamati, E. Toussaint, D. Turner, C. S. R. Vemulapati, T. Weikert, J. F. Witz, O. Witzel, and J. Yang. DIC challenge 2.0: Developing images and guidelines for evaluating accuracy and resolution of 2D analyses. *Experimental Mechanics*, 2022. Accepted, online.
- [44] J. Yang., J. L. Tao, and C. Franck. Smart digital image correlation patterns via 3d printing. *Experimental Mechanics*, 61(7):1181–1191, 2021.
- [45] Y. Su and Q. Zhang. Glare: A free and open-source software for generation and assessment of digital speckle pattern. *Optics and Lasers in Engineering*, 148:106766, 2022.
- [46] F. Sur, B. Blaysat, and M. Grédiac. Rendering deformed speckle images with a Boolean model. *Journal of Mathematical Imaging and Vision*, 60(5):634–650, 2018.

- [47] B. Blaysat, M. Grédiac, and F. Sur. Effect of interpolation on noise propagation from images to DIC displacement maps. *International Journal for Numerical Methods in Engineering*, 108(3):213–232, 2016.
- [48] P. Reu. Speckles and their relationship to the digital camera. *Experimental Techniques*, 38(4):1–2, 2014.
- [49] P. Reu. All about speckles: Contrast. *Experimental Techniques*, 39(1):1–2, 2015.
- [50] A. Vinel, R. Seghir, J. Berthe, G. Portemont, and J. Réthoré. Metrological assessment of multi-sensor camera technology for spatially resolved ultra-high speed imaging of transient high strain-rate deformation processes. *Strain*, 2021. accepted, online.
- [51] M. Grédiac, F. Sur, and B. Blaysat. Comparing several spectral methods used to extract displacement and strain fields from checkerboard images. *Optics and Lasers in Engineering*, 127:105984, 2020.
- [52] S. Qin, M. Grédiac, B. Blaysat, S. Ma, and F. Sur. Influence of the sampling density on the noise level in displacement and strain maps obtained by processing periodic patterns. *Measurement*, 173:108570, 2021.
- [53] R. Fedele, L. Galantucci, and A. Ciani. Global 2D digital image correlation for motion estimation in a finite element framework: a variational formulation and a regularized, pyramidal, multi-grid implementation. *International Journal for Numerical Methods in Engineering*, 96(12):739–762, 2013.
- [54] N.I. Muskhelishvili. *Some basic problems of the mathematical theory of elasticity*. 1957.
- [55] Q. Bouyra, B. Blaysat, H. Chanal, and M. Grédiac. Using laser marking to engrave optimal patterns for in-plane displacement and strain measurement. *Strain*, 2021. Accepted, online. DOI: <https://doi.org/10.1111/str.12404>.